VTT Technical Research Centre of Finland

Effects of Surface Treatments on Environmentally-Assisted Cracking Susceptibility of Alloy 182 in BWR Environment

Que, Zaiqing; Volpe, L.; Toivonen, Aki; Burke, M.g.; Scenini, Fabio; Ehrnstén, Ulla

Published in:
Corrosion Science

DOI:
10.1016/j.corsci.2021.109555

Published: 01/08/2021

Document Version
Publisher's final version

Corrosion Science 188 (2021) 109555

Contents lists available at ScienceDirect

Corrosion Science

journal homepage: www.elsevier.com/locate/corsci

Effects of surface treatments on environmentally-assisted cracking susceptibility of Alloy 182 in BWR environment

Z. Que [a,*,1], L. Volpe [b,*,1], A. Toivonen [a], M.G. Burke [b], F. Scenini [b], U. Ehrnstén [a]

[a] Nuclear Reactor Materials, VTT Technical Research Centre of Finland, Kivimiehentie 3, P.O. Box 1000, FI-02044, VTT, Finland
[b] Materials Performance Centre, Department of Materials, University of Manchester, Oxford Road, M13 9PL, Manchester, UK

ARTICLE INFO

Keywords:
Alloy 182
Environmentally-assisted cracking
Stress corrosion cracking
Surface machining
Characterisation

ABSTRACT

The effects of four machining surface preparations on the environmentally-assisted cracking (EAC) initiation and early crack growth were evaluated for Alloy 182 flat tapered specimens exposed to a simulated boiling water reactor (BWR) environment under constant extension rate tensile test conditions. Results showed that the apparent EAC critical threshold stress for initiation was highly dependent on the surface treatment. Detailed microstructural characterization revealed the nature of the machining-induced deformation associated with the four surface treatments. Surface treatments affected the surface oxidation during exposure in the simulated BWR environment. The machining-induced deformation structure affected the EAC initiation susceptibility.

1. Introduction

Alloy 182 is widely used in nuclear power plants as a filler metal for welds between Ni-base alloys, austenitic stainless steels and low-alloy steels [1,2]. However, Alloy 182 is susceptible to intergranular stress corrosion cracking (IGSCC) under boiling water reactor (BWR) conditions [3–5] and to environmentally-assisted cracking (EAC) in high temperature water [6–9]. The development of EAC can be described as consisting of two stages: 1) initiation, which is subdivided into precursor events, crack incubation, and the formation of short cracks; and 2) propagation in which rapid crack growth occurs [10].

It is well known that machining or industrial operations can have a strong impact on the EAC susceptibility of the material [11–14]. For example, both plant operation experience and laboratory tests have shown that cold work could significantly enhance the crack growth in austenitic stainless steels in high temperature water environments [15,16], and that hardening of the materials by cold work can lead to a local increase in yield stress and strain [11]. Surface machining is an indispensable finishing procedure in the industrial fabrication of nuclear components that results in heavily cold-worked surfaces [12].Various treatments have been applied in order to mitigate the occurrence of EAC in Alloy 182, such as peening [17] or laser surface melting [18].

However, to date there are insufficient results on the effect of machining on the early stages of EAC for Alloy 182, and therefore to obtain large dataset in a relatively short time, constant extension rate tensile (CERT) tests were used on Alloy 182 flat tapered specimens [19]. In fact, the geometry of these specimens enables to extrapolate the value of threshold stress from one single specimen, rather than perform different experiment at different stress values. The minimum stress threshold was evaluated from the location of the last EAC crack along the gauge length [19,20].

In this study, the EAC initiation and early crack growth in A182 were studied as function of three industrial surface machining processes and compared to a reference surface (RS) prepared with a P2000 grit paper. This work was focused on assessing: 1) the apparent critical threshold stress for each surface process, and 2) the oxidation behaviour and crack development as function of the surface machining, which were characterized using variety of electron microscopy-based techniques. Specifically, the results obtained from the CERT tests will be used as pre-step for upcoming constant load experiments. This study was performed under the EU Horizon 2020 project “Mitigating Environmentally-Assisted Cracking Through Optimisation of Surface Condition” (MEACTOS) with the ultimate goal of developing optimized processing for improved EAC performance of materials in light water reactors [21].

* Corresponding authors.
E-mail addresses: zaiqing.que@vtt.fi (Z. Que), liberato.volpe@manchester.ac.uk (L. Volpe).
[1] First authors.

https://doi.org/10.1016/j.corsci.2021.109555
Received 18 January 2021; Received in revised form 6 May 2021; Accepted 12 May 2021
Available online 15 May 2021

Table 1
Chemical composition (wt.%) of Alloy 182 overlay.

Ni	Cr	Mn	Fe	Nb	Si	Ti	Mo	Cu	Co	C	Al	S
66.1	14.6	6.31	9.4	1.97	0.59	0.252	0.13	0.043	0.033	0.032	0.019	0.01

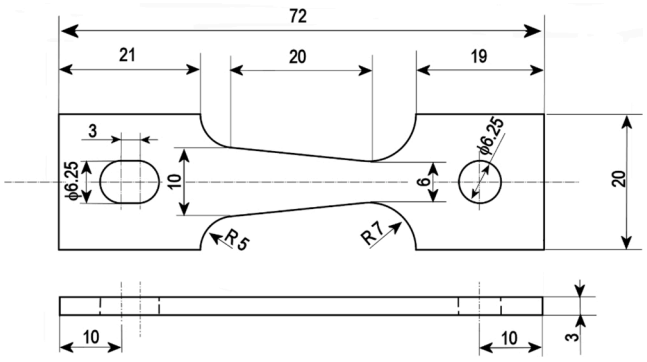

Fig. 1. Schematic of the A182 flat tapered specimen used for CERT test, where the dimensions are in mm.

2. Materials and experimental procedures

2.1. Materials and specimens

Alloy 182 was provided by ENSA as a multi-pass deposit on an Alloy 82-clad low alloy steel plate. A weld overlay technique was used by ENSA to deposit the Alloy 182 layers, and this was followed by post-weld heat treatment (~600 °C/15 min). The thickness of the Alloy 182 overlay was between 10 and 11 mm. The Alloy 182 chemical composition was analysed with optical emission spectrometry and is reported in Table 1. The orientation of the flat tapered specimens used in this study was T-S. Flat tapered specimens with dimensions of 3 mm thickness, 6 mm minimum width, 10 mm maximum width over a 20 mm gauge length were extracted using electrical discharge machining (EDM) from the Alloy 182 overlay by the Nuclear Advanced Materials Research Centre (NAMRC) and ENSA. A schematic diagram with the comprehensive dimensions is shown in Fig. 1. Additional miniature flat tapered specimens (3 mm thickness, 3 mm minimum width, 5 mm maximum width with 14 mm gauge length) were prepared and used to study the effect of specimen size on EAC threshold stress for comparison with the standard specimen test results. The ratio between the gauge length and minimum and maximum cross-sections was the same for the standard and miniature flat tapered specimens. The flat tapered specimens were carefully rinsed with ethanol and soapy water to remove any residual oils used during the machining preparation.

The use of a flat tapered samples evidences that not only the strain but also the strain rate varies over the gauge length. The strain and the strain rate are highest in the narrowest cross-section region and they decrease as the cross section increases. The strain and strain rate distribution over the gauge length were calculated using the Ramber-Osgood approximation [20,22] of the constitutive law that best fit the tensile data of the stress-strain curve at the test temperature. The last EAC cracks were normally observed ~15 mm away from the narrowest cross-section of the tapered sample, which were located in a region with a strain of ~2% and a strain rate of $\sim 2 \times 10^{-8}$ s^{-1} at the end of the CERT test for a nominal strain rate of 1×10^{-7} s^{-1}. At the position of the final EAC crack, the real strain rate was lower than the nominal average strain rate. To simplify the discussion, the nominal strain rate that was calculated from the whole gauge length is used in the text.

2.2. Surfaces treatments

The flat tapered specimens were provided with four different surface treatment processes. For each specimen, one surface was ground with a SiC P2000 grit paper, corresponding to a 1000 grit (with a nominal SiC size of 10 μm) that was used as the reference surface (RS). The opposite face was machined with specific surface treatments, the main parameters of which are reported below. Each tapered specimen was labelled with a specific Part Number (P/N) as reported in Table 2.

1 Surface Treatment Industrial (STI): The STI finish was performed by flat milling with a feed speed of 300 mm/min, cut depth of 0.5 mm, overlap ratio of 70 % and tool rotation speed of 200 min^{-1}.
2 Surface Advanced Machining (SAM): This cryogenic machining process was applied with a Starrag HEC 1800 machining centre that uses a flow rate of 37.2 kg/h of super-cooled CO_2 as coolant and 1 mL/min of oil lubrication in face milling. The cutting tool that was used is an Ø36 mm 419 series face mill (419−036C3-14 L). The SAM finish was performed with a feed speed of 0.3 mm/tooth, a depth of cut of 0.5 mm and a cutting speed of 52 m/min. SAM has been proposed as an alternative solution for the future machining needs for nuclear reactor components [23].
3 Shot Peening (SP): The shot peening process was applied on a rough ground (SiC 80 grit paper) surface and it was performed with ceramic balls with diameter of 600 μm and a kinetic energy (Almen intensity tolerance) of F25-35A. The coverage (ratio of impacts on the surface) was 125 %. Compressive stress beneath the surface as a result of plastic deformation was elastically constrained by the surrounding

Table 2
Summary of apparent EAC initiation threshold stress analysis for as deposited Alloy 182 tapered specimens after exposure to simulated BWR under CERT condition.

Specimen Part Number	Surface	Nominal strain rate, s^{-1}	Tested till	Maximum load, kN	Maximum stress, MPa	Crit. spec. width, mm	Crit. spec. thickness mm	Crit. Area, mm^2	Apparent crit. stress threshold MPa
1A17S	RS	1×10^{-6}	Rupture	10.3	612	6.8	3.0	20.1	511
	STI					7.1	3.1	21.7	473
1A3S	RS	5×10^{-6}	UTS	11.4	613	7.9	3.0	23.9	475
	STI					8.2	3.1	25.2	452
1A4S	RS	1×10^{-7}	UTS	11.3	582	8.4	3.1	26.1	433
	STI					8.1	3.1	25.3	448
1B14S*	RS	1×10^{-7}	Rupture	5.7	641	4.3	3.1	13.2	433
	STI					4.2	3.1	12.7	451
2A3C	RS	1×10^{-7}	Rupture	12.0	673	8.9	3.1	27.7	431
	SAM					8.2	3.1	25.5	469
3A5PS	RS	1×10^{-7}	Rupture	10.6	583	7.7	3.1	23.8	447
	SP					9.3	3.1	28.9	368

* Miniature size.

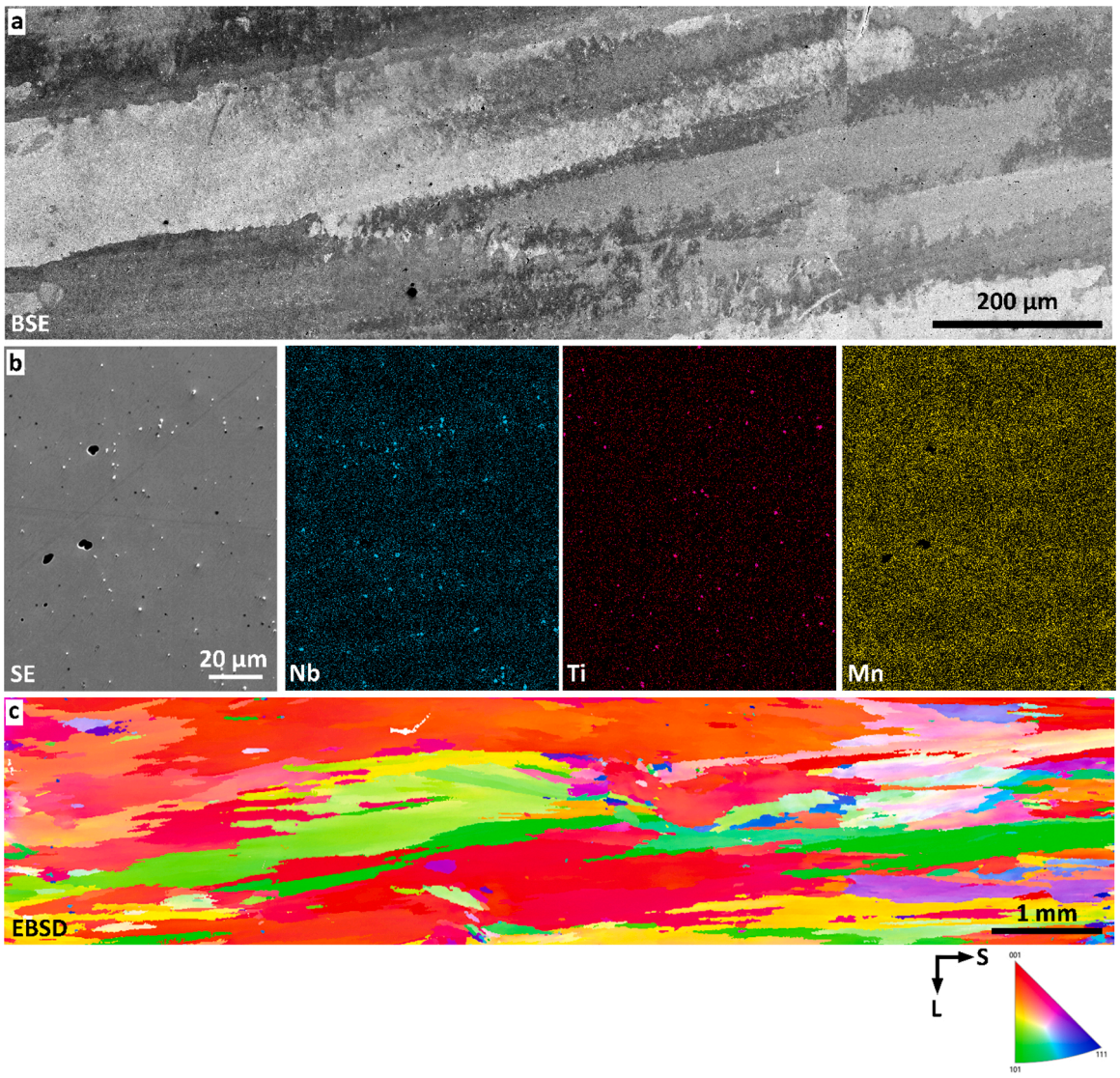

Fig. 2. (a) Montage BSE of the Alloy 182 multi-bead deposit along the L-S plane showing the elongated grain structure along the S direction. (b) Higher SE image and corresponding EDX elemental maps for Nb, Ti and Mn. Note the pronounced elemental partitioning for Mn and Nb in the A182 deposit and the presence of numerous Nb- and Ti-rich inclusions in the interdendritic regions. (c) EBSD IPF map confirming the elongated grain structure for the Alloy 182 on the L-S plane.

material [24]. The SP treatment was included in the test matrix for a pre-study on the applicability of the CERT technique for peened surfaces relevant for nuclear applications, *e.g.* cavitation peening.

2.3. Experimental procedures

The flat tapered samples were tested under CERT conditions with a nominal strain rate equal to $1 \times 10^{-6}\,s^{-1}$, $5 \times 10^{-7}\,s^{-1}$ and $1 \times 10^{-7}\,s^{-1}$ in simulated BWR NWC environment at 288 °C. The tests were conducted in recirculating autoclaves from Cormet, Ltd. The simulated light water reactor coolant chemistry was controlled by a water recirculation loop built by VTT. Oxidizing BWR NWC was created by using neutral high-purity water with a $pH_{288\,^\circ C}$ equal to 5.7 and an inlet conductivity of 0.055 µS/cm at which 2 ppm oxygen were added (+100 mV_{SHE}). The specimens were loaded into the autoclave, pre-oxidized for 168 h at 288 °C to create a homogeneous oxide film, and then the strain was applied. The tests were stopped upon final failure (rupture) or above the ultimate tensile stress as reported in Table 2.

2.4. Microstructural characterization

2.4.1. Sample preparation

Alloy 182 excess materials with the different surface machining processes were used for analysis of the bulk and near-surface microstructures. The characterization of the post-test tapered tensile specimens was performed on cross-section samples. The A182 excess materials with the RS/STI/SAM and SP surface finishes and the flat tapered samples were cross-sectioned with a blade saw, mounted in Bakelite resin, ground and metallographically polished (0.2 µm). The final polishing step was performed using a 0.04 µm non-crystallizing amorphous colloidal silica suspension (OPS) to ensure a strain-free surface.

2.4.2. Advanced microstructural characterization

The specimens were characterized before and after exposure to the simulated BWR NWC environment using several complementary electron microscopy techniques such as scanning electron microscopy (SEM), focused ion beam (FIB) microscopy, and analytical transmission electron microscopy (ATEM).

A Zeiss Merlin field emission gun - scanning electron microscope

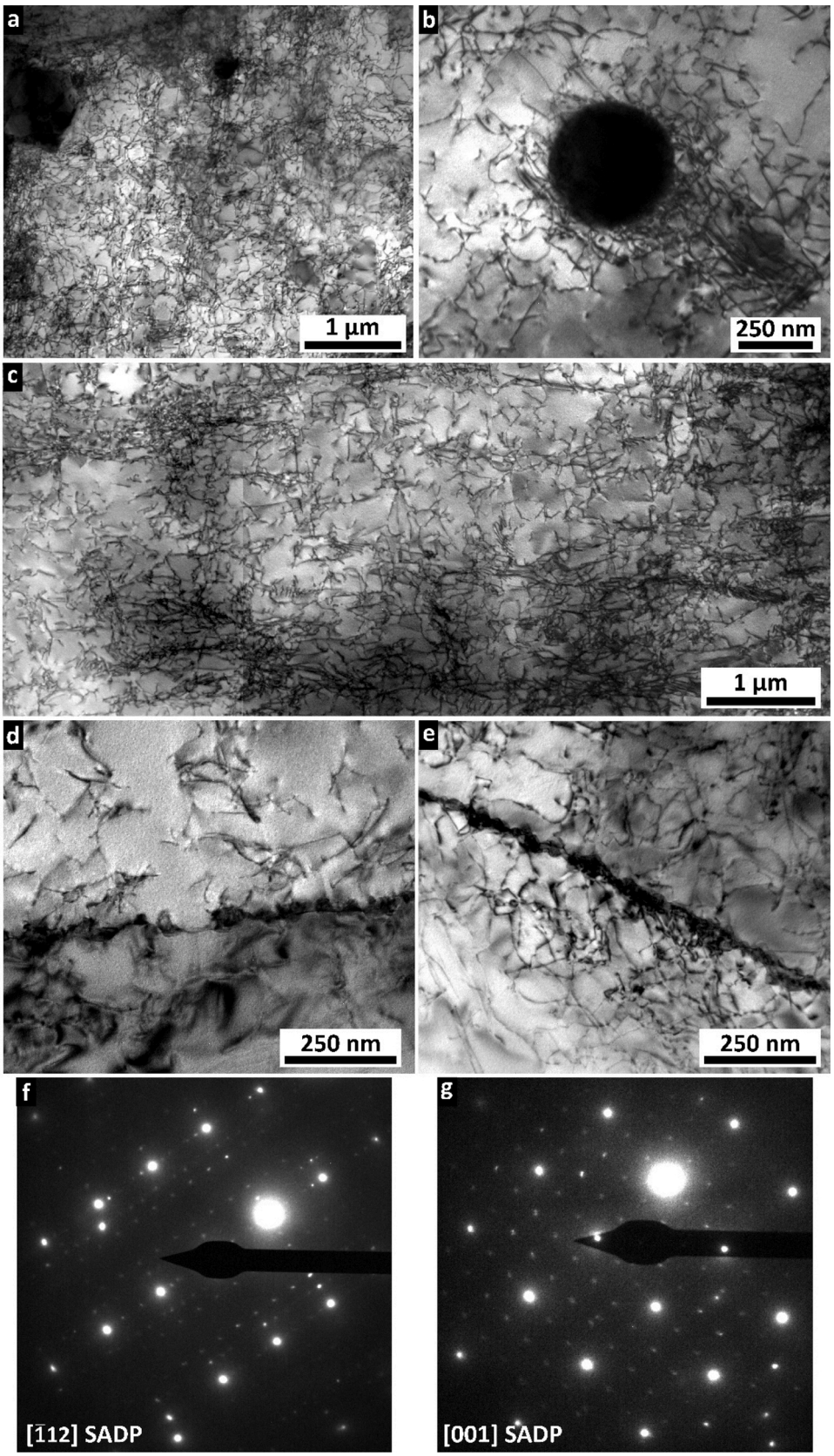

Fig. 3. (a) low magnification and (c) montage BF TEM images showing the typical dislocation structures in the stress-relieved Alloy 182. (b) higher magnification BF TEM image of a spheroidal oxide inclusion formed during the deposition. (d) BF TEM micrograph and associated (f) [112] SADP showing the presence of intergranular MC. (e) BF TEM image and associated (g) [001] SADP showing the presence of $M_{23}C_6$ intergranular carbides.

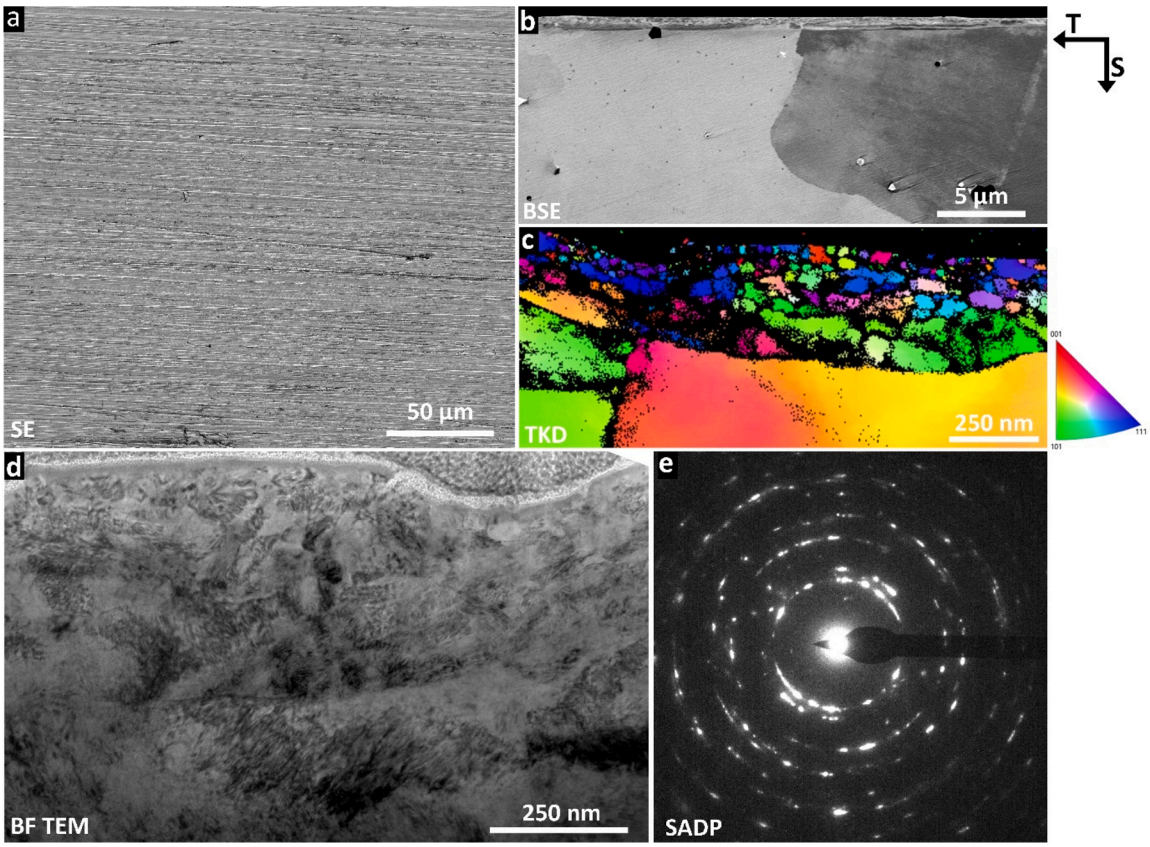

Fig. 4. (a) SE image showing a portion of the surface after RS grinding process with associated deformed region on the T-S plane shown in the (b) BSE image. (c) TKD analysis of the top ~500 nm of the UFG layer showing grain sizes from ~15 to ~250 nm. (d) BF TEM image of the UFG layer with (e) corresponding SADP showing a randomly-oriented UFG polycrystalline layer.

(FEG-SEM) equipped with two Oxford Instruments (OI) X-max 150 silicon drift detectors (SDDs) for standard energy dispersive X-ray (EDX) microanalysis, and an OI X-max Extreme 100 windowless SDD for low voltage (less than 5 kV) EDX analysis was used to assess the chemical composition of the surface oxides. The benefit of low voltage SEM-EDX microanalysis is that the EDX data are generated from a narrow depth (~80 nm or less) beneath the surface, thereby generating compositional data from near-surface layer. The SEM-EDX spectrum image (SI) datasets were acquired with a dwell time of 150 µs per pixel for a total live time of 30 min with a pixel size equal to 36.44 nm. SEM-EDX SI datasets of 512 × 384 px^2 were subsequently analysed using the OI Aztec software (ver. 4.0) and the data were background subtracted and processed using True Map™ software. A Zeiss Sigma FEG-SEM equipped with an (OI) X-max 150 SDD for standard EDX microanalysis and an EBSD detector was operated at 20 kV with a current of 1.5 nA to obtain the EBSD map of the baseline bulk microstructure of the as-deposited Alloy 182. The map was obtained with a step size of 4 µm and acquired and processed with the OI Aztec software (ver. 4.0).

A FEG-SEM Zeiss Crossbeam 540 equipped with an EDAX Hikari Plus EBSD detector and solid-state four-quadrant backscatter electron (BSE) detector were used to characterize the surfaces as well as the narrowest and widest cross-section regions of the tested specimens. EBSD analysis was conducted at 15 kV acceleration voltage and working distance of 14 mm with a 70° tilting angle and a probe current of 1.5 nA. The step size for acquisition of EBSD maps in this work was 30 nm (except for EBSD analysis of the entire through-thickness of the Alloy 182 overlay cross-section, which used a 300 nm step size). EBSD inverse pole figures (IPF) and kernel average misorientation (KAM) images with scale of 0–5° were analysed using the TSL OIM Analysis 8 software. Dislocation structures adjacent to the surface of tested samples was examined using the electron channelling contrast of the BSE image. BSE channelling contrast has the advantage of using bulk specimens and can access much larger area, though the resolution is lower than that for TEM analysis. BSE imaging was performed at 20 kV acceleration voltage with working distance of 5–6 mm using the solid-state four-quadrant BSE detector.

An FEI Helios 660 Nano Lab FEG FIB/SEM was used to obtain BSE micrographs of the Alloy 182 overlay and to prepare electron-transparent cross-section TEM lift-out samples from the grip portion of the flat tapered samples prior to exposure in the BWR environment. The TEM samples were extracted using the *in situ* lift-out technique for the Alloy 182 specimens with RS, STI, SAM and SP surface conditions, thinned to electron-transparency with a final polish at 2 kV to minimize the curtaining effect produced by the Ga^+ ion beam. Transmission Kikuchi diffraction (TKD) analyses were performed using the Zeiss Merlin FEG-SEM was operated at 30 kV with a current of 1.5 nA and a step size of 50 nm on the electron-transparent FIB lift-out specimens extracted from the RS, STI, SAM and SP specimens that included the ultrafine-grained (UFG) layer in the near-surface machined region.

These thinned specimens were also examined in an FEI Tecnai T20 G2 analytical TEM/STEM operated at 200 kV and equipped with an OI X-Max 80TLE windowless SDD EDX detector. Further ATEM analyses were also performed on conventional electropolished TEM specimens to obtain information regarding the as-deposited A182 baseline bulk microstructure. These specimens were prepared from 3.0 mm diameter ×100 µm thick disc samples extracted on the L–T plane, electropolished in 20 % $HClO_4$ – 80 % CH_3OH electrolyte at −33 °C with a Struers Tenupol 5 equipped with a Jubalo closed-cycle refrigeration system.

2.5. Stress threshold evaluation

The last EAC crack and associated distance I_{EAC} (in tensile direction only) from the wide end of the flat tapered specimen were determined

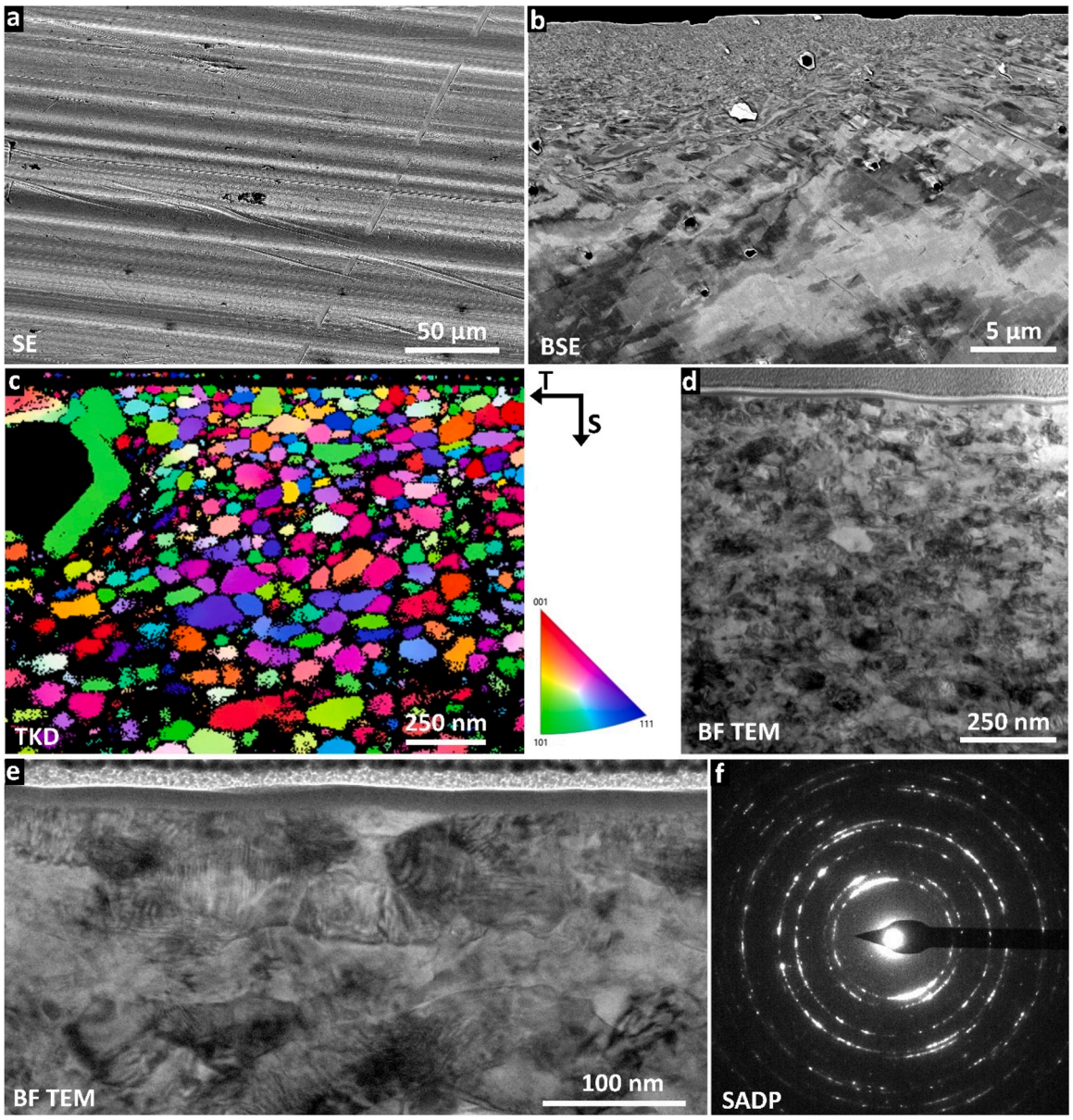

Fig. 5. (a) SE image showing a portion of the surface after the STI machining process with associated UFG and deformed region on the T-S plane shown in the (b) BSE image. (c) TKD analysis of the top ~1 µm of the UFG layer showing grain sizes from ~15 to ~200 nm. (d) BF TEM image of the UFG layer and (e) higher magnification BF TEM image showing the of several fringes associated with plastically deformation. In (d), the corresponding SADP showing a randomly-oriented UFG polycrystalline layer.

for each surface of the specimen. A crack was defined as a valid EAC when: i) the crack was approximately 20 µm in extent, ii) the crack was generally straight, and iii) the crack orientation roughly perpendicular to the axis of stress. Cracks were imaged at a magnification of ×500 (or a field-of-view of 230 × 170 µm^2). For each known distance I_{EAC}, the corresponding specimen width at the position I_{EAC} at the same specimen before the CERT test (on the non-strained specimen) was determined. The thickness at the position I_{EAC} is determined from the sample after the CERT test (strained specimen). From these two dimensions the critical cross-section area A_{crit} was obtained and the maximum load was obtained from the load-displacement curve. The stress threshold was then calculated by dividing the maximum load by the critical cross-section area, for each side of the specimen.

3. Results

3.1. Baseline microstructural characterization of the specimens

The A182 overlay deposit was evaluated using several complementary analytical techniques to assess the general microstructure of this material. These analyses revealed a coarse dendritic solidification microstructure with some dendrites of several mm in length on the L–S plane, as shown in the BSE micrograph in Fig. 2(a). The elemental maps extracted from the SEM-EDX (Fig. 2(b)) spectrum image datasets revealed elemental partitioning in the A182 overlay deposit that was consistent with micro-segregation generally observed in an A182 weld. The darkly-imaging features in the secondary electron (SE) image in Fig. 2(b) were voids associated with a possible pull-out of inclusions during metallographic preparation. Similarly, the interdendritic Nb-rich and Ti-rich features are consistent with the coarse carbide and nitride inclusions typically observed in A182 welds. The interdendritic

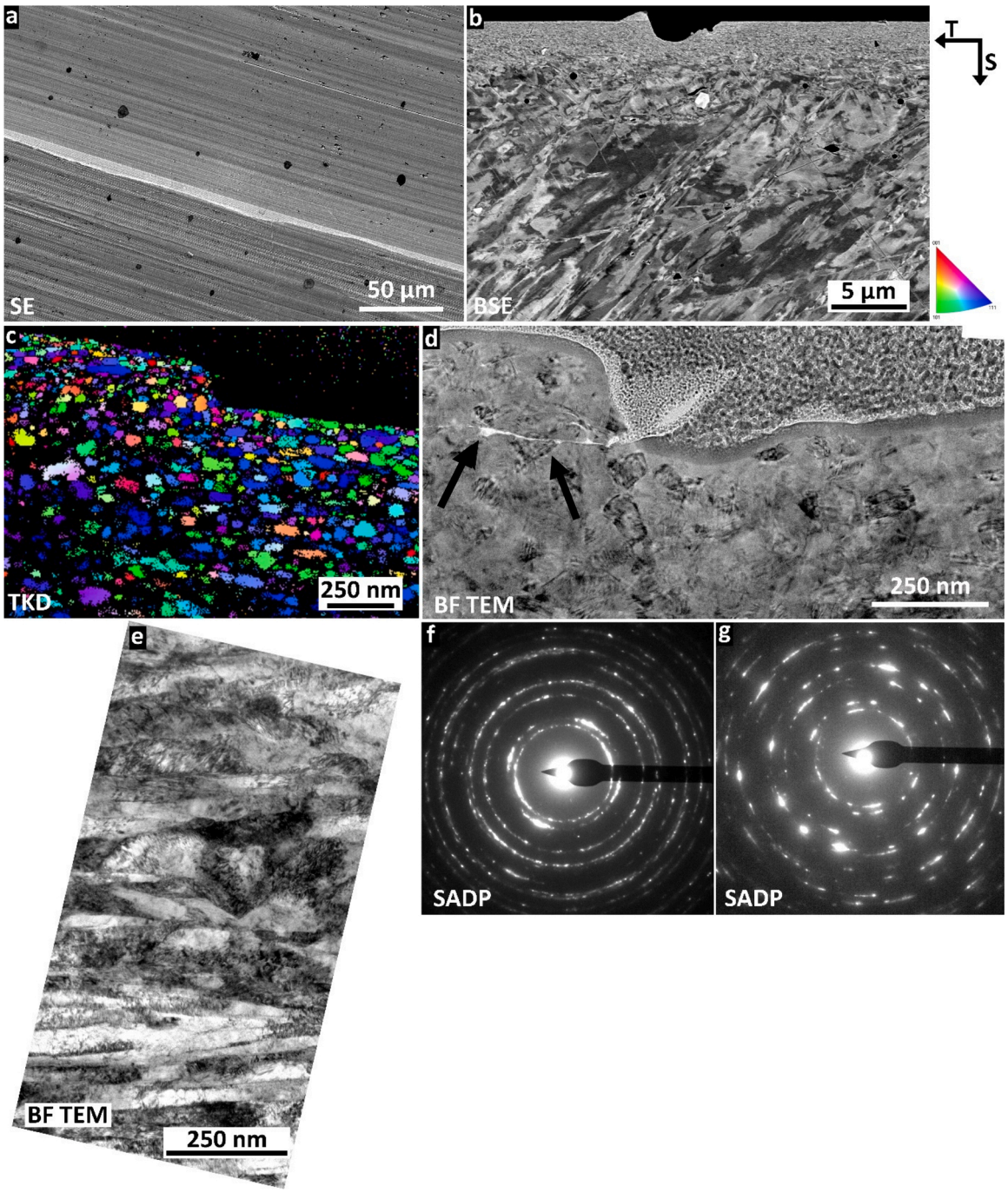

Fig. 6. (a) SE image showing a portion of the surface after the SAM machining process with associated UFG and deformed region on the T-S plane shown in the (b) BSE image. Note the presence of a defect associated with the machining process. (c) TKD analysis of the top ~1 µm of the UFG layer showing grain sizes from ~15 to ~100 nm. (d) BF TEM image of SAM cross-section containing a micro-lap (black arrow) and (g) BF TEM image showing the elongated/"pancaked" deformed grains beneath the UFG layer. (f) SADP of randomly-oriented UFG layer and (g) SADP of sub-UFG deformed layer with elongated / "pancaked" highly deformed grains.

structure was also confirmed by EBSD analysis, as shown in Fig. 2(c).

TEM characterisation of this stress-relieved A182 overlay deposit revealed a highly dislocated microstructure containing coarse non-uniformly distributed NbC as well as some Ti-rich nitrides and spheroidal oxides, as shown in the bright field (BF) TEM micrographs in Fig. 3(a – c). TEM analysis also confirmed the presence of Nb-rich MC carbides (Fig. 3(d and f)) and intergranular (IG) $M_{23}C_6$ carbides (Fig. 3(e and g)).

3.2. *Microstructural characterization of the as-machined/as-treated specimens*

3.2.1. *RS condition*

The SE micrograph in Fig. 4(a) shows the surface after the RS grinding process (T-L plane). The grinding marks appears to be parallel to the T direction and no major defect were visible. The grinding process induced a limited deformed region, as visible in the BSE image in Fig. 4 (b). The deformed region was formed by an UFG layer less than 200 nm deep as shown in the TKD map in Fig. 4(c). The BF TEM image (Fig. 4(d)) and corresponding SADP (Fig. 4(e)) confirmed the UFG layer.

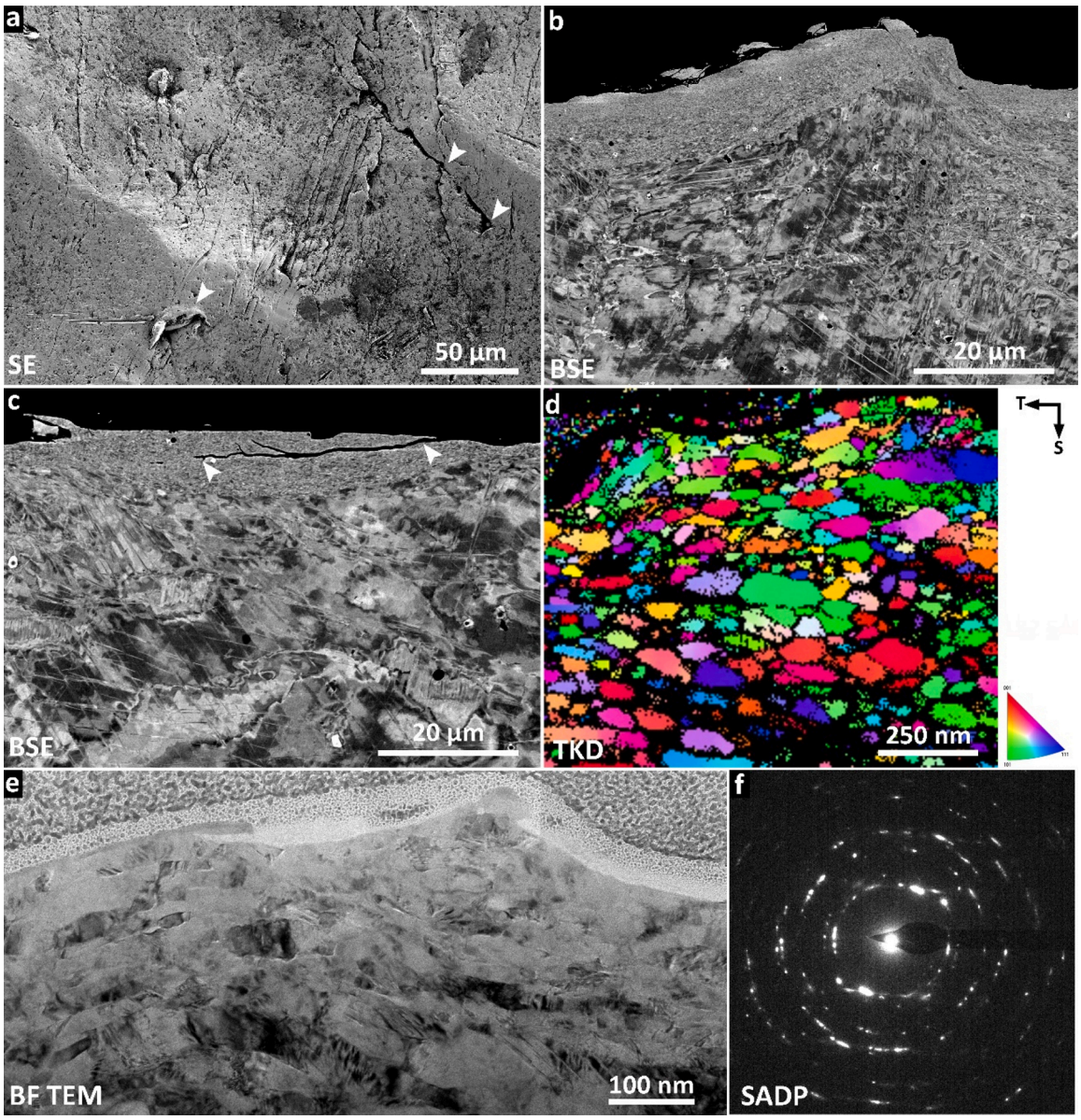

Fig. 7. (a) SE image showing a portion of the highly damages surface after the SP. The (b) BSE image shows the complex microstructure formed after the process just beneath the surface on the T-S plane with the (c) formation of crack within the UFG layer as shown in the BSE image. (c) TKD analysis of the top ~1 µm of the UFG layer showing grain sizes from ~15 to ~250 nm. (e) BF TEM image of the UFG layer with (f) corresponding SADP showing a randomly-oriented UFG polycrystalline layer.

3.2.2. STI machined condition

A representative SE micrograph of the surface after the STI industrial machining process is shown in Fig. 5(a). The surface was decorated with machining marks and spheroidal darkly-imaging features, possibly associated with oil contamination from the machining process. The STI process induced the formation of a 2–4 µm deep UFG layer with an underlying deformed region, as shown in the BSE micrographs in Fig. 5 (b). TKD analysis (Fig. 5(c)) performed on the electron-transparent specimen revealed that the nanograins ranged from ~15 to 200 nm in size. Examination of Fig. 5(c) also revealed the presence of an inclusion on the upper left corner surrounded by a highly deformed region. The BF TEM image of the UFG layer (Fig. 5(d) with the corresponding SADP (Fig. 5(f)) shows a randomly-oriented UFG polycrystalline layer. A higher magnification BF TEM montaged image (Fig. 5(e)) shows the presence of a thin ~20 nm amorphous surface layer (C contaminant from machining) and the presence of fringes in the nanograins associated with a plastically deformed region.

3.2.3. SAM machined condition

Similar results were obtained for the SAM surface machining process, as shown in Fig. 6. The topographic SE micrograph in Fig. 6(a) show the machining marks and the spheroidal darkly imaging features randomly distributed on the T–L surface. The SAM machining process induced the formation of the UFG layer and deformed region, clearly visible in the BSE image in Fig. 6(b). TKD analysis presented in Fig. 6(c) shows the ultrafine grains (~15 to 150 nm in size) in the ~1 µm deep region beneath the surface. Further and more detailed BF TEM examination of the near-surface region of the SAM-machined sample revealed a two-layer structure: 1) an outermost randomly-oriented UFG layer with nano-scale grains (Fig. 6(d)), as evidenced by the SADP (Fig. 6 (f)); and 2) a fine-grained layer with elongated/"pancaked" deformed grains >200 nm in length (Fig. 6(e)) with a more oriented grain structure (as revealed also by the SADP in Fig. 6(f)). Additionally, in the BF TEM in Fig. 6(d), a micro-lap is evident and indicated by the black arrow. The extent of deformation of the "pancaked" grains is clear not only in the

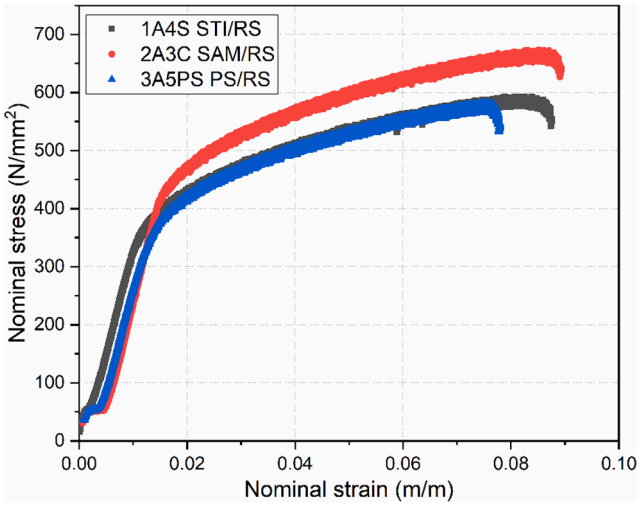

Fig. 8. Strain-stress curves of the CERT tests with flat tapered specimens with different surface treatments tested at nominal strain rate of 1×10^{-7} s^{-1} in simulated BWR NWC environment at 288 °C, 1A4S (black squares), 2A3C (red circles), 3A5PS (blue triangle-up). The nominal strain was calculated by $\Delta L/L_0$, where L_0 is the original gauge length (20 mm). The nominal stress was calculated by load/A_0, where A_0 is the original minimal gauge cross section.

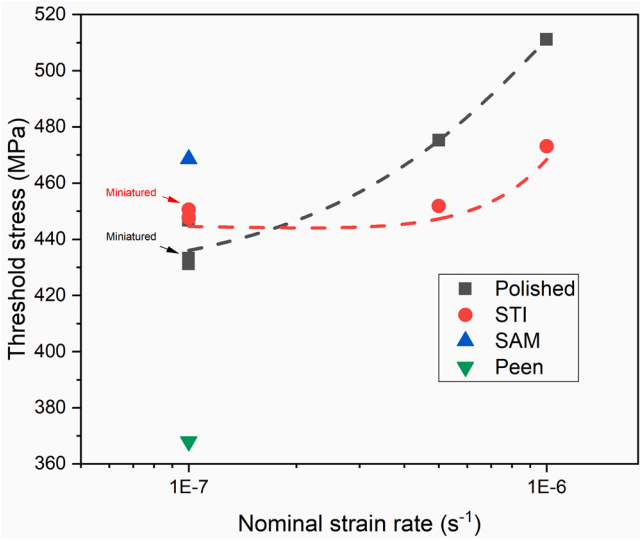

Fig. 9. Summary of the apparent EAC initiation threshold stress as function of the nominal strain rate obtained from the CERT experiments performed on the Alloy 182 tapered specimens in BWR NWC environment at 288 °C with different surface machining treatments: RS (black squares), STI (red circles), SAM (blue triangle-up), SP (inverted green triangle).

BF-TEM image in Fig. 6(e) but also in the "smeared" reflections in the associated SADP in Fig. 6(f).

3.2.4. SP condition

The SE characterization of the as-shot-peened (SP) A182 sample surface revealed a pronounced cratered surface with cracks (white arrows in Fig. 7(a)), as expected for this treatment. BSE micrographs of the near-surface region revealed the complex microstructure formed after the peening process with the formation of an UFG layer ranging from ~2 μm and ~10 μm in depth (Fig. 7(b)) as well as the formation of cracks in the UFG layer (Fig. 7(c)). The UFG layer produced by the SP process contained grains ranging from ~15 to ~250 nm in size as shown in the TKD image in Fig. 7(d), with some elongated (pancaked) grains. The BF TEM montaged image in Fig. 7(e) and the corresponding SADP in Fig. 7(f) confirmed the pancaked nano-scale grains beneath the peened surface.

3.3. EAC initiation: CERT results

Fig. 8 shows the strain-stress curves of the CERT tests with flat tapered specimens with different surfaces tested at a nominal strain rate of 1×10^{-7} s^{-1} in simulated BWR environment. The 3A5PS specimen (SP/RS) had the lowest strain when reaching the UTS. The 2A3C specimen (SAM/RS) had a higher UTS compared to 1A4S specimen (STI/RS) with a similar strain level.

Fig. 9 shows the evolution of the calculated apparent EAC initiation threshold stress analysis for the tapered specimens as function of the nominal strain rates and surface treatment conditions. The calculated apparent EAC initiation threshold stress increases with the test strain rate. At a nominal strain rate of 1×10^{-6} or 5×10^{-6} s^{-1}, the RS surface had a stronger resistance to EAC initiation than STI surface. At a nominal strain rate of 1×10^{-7} s^{-1}, SAM had a highest EAC initiation threshold stress. The apparent EAC initiation threshold stress at 1×10^{-7} s^{-1} was found following the sequence of SAM > STI > RS > SP. The threshold stress value of the miniature specimen was consistent with the stress threshold values obtained by the standard size specimen, and therefore indicated no influence of specimen dimensions of EAC initiation stress threshold.

3.4. Microstructural characterization of the surfaces after exposure to BWR environment

Representative SE micrographs of the outer oxide layer on the specimens tested at a nominal strain rate of 1×10^{-7} s^{-1} in simulated BWR environment with the four different surface treatments are shown in Figs. 10 and 11. Specifically, the micrographs in Fig. 10 were acquired in the proximity of the widest cross-section, which had lowest stress whereas the Fig. 11 images were acquired in the proximity of the narrowest cross-section, which experienced the highest stress during loading. SE micrographs in Fig. 10 show that the surface was covered with an external oxide that consisted of a uniform fine-grained oxide layer with some coarse discrete oxide crystals. An oxide layer formed by fine and interconnected flakes (smaller than 0.5 μm) is visible in the higher magnification images in Fig. 10(b, d, f, h). Coarse spheroidal oxides (~1–6 μm) are visible on RS and STI surfaces in Fig. 10(a, c). On SP surface, there is a mixture of flake-like oxides with some non-uniformly distributed long, coarse filamentous features evident in low magnification images (Fig. 10(g)).

In the proximity of the narrowest cross-sections in Fig. 11, the RS, STI and SAM surface were covered with a uniform, fine oxide layer without coarse discrete crystals (Fig. 11(a, b, c)). On the SP surface, the long filamentous features were observed on top of the uniform surface oxide (Fig. 11(d)).

As noted above, the SP surface has a distinctly different filamentary deposit on oxidized surfaces. Low voltage SEM-EDX spectrum image datasets were obtained from these regions to generate elemental maps within ~80 nm of the SP specimen surface, which are shown in Fig. 12. These analyses revealed that the coarse deposited particles and the long filamentous features were mainly composed of Fe- and Ni-rich oxides with trace of Al (~0.5 wt. %). The sum spectrum associated with the SEM-EDX spectrum image dataset for Fig. 12 is shown in Fig. 13, thus confirming the presence of Al (Al Kα) and Si (Si Kα) in these features.

The SE images of the last identified "cracks" on the tapered gauge length for the various surfaces are shown in Fig. 14. The calculated apparent EAC initiation critical stress threshold based on the crack location beyond which there were no cracks observed on the surface-treated tapered specimens was intended to provide a general trend and comparison of the EAC susceptibility for the various surface treatments. The summary of apparent EAC threshold stress analysis of the tapered post-CERT specimens is shown in Table 2. In this table, the

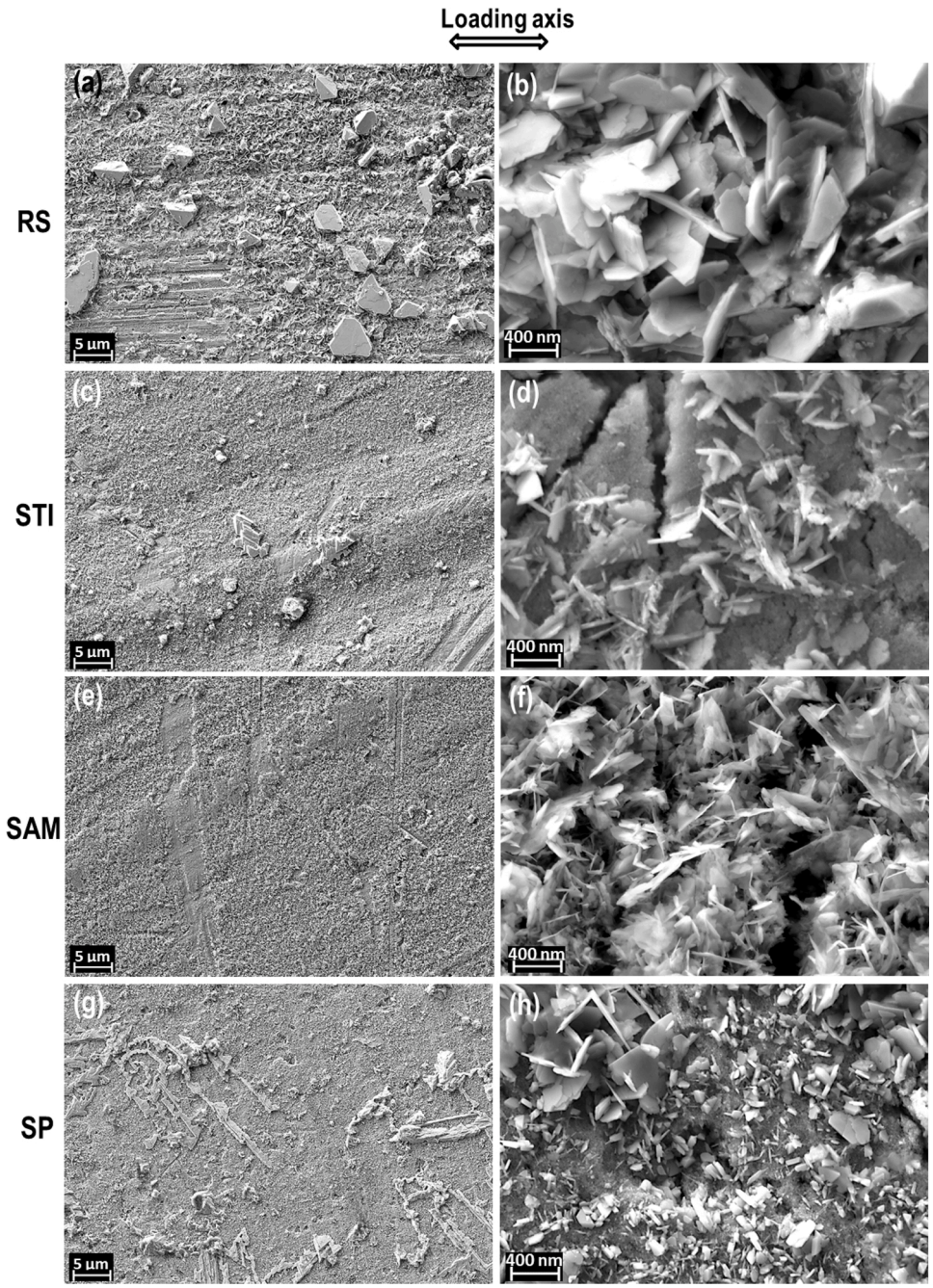

Fig. 10. SE images of the outer oxide layer observed on the widest portion of the gauge length (lowest strain) on the post-CERT-tested specimens exposed to simulated BWR environment as a function of surface treatment. (a, b) RS surface (P/N 1B14S); in (c, d) STI surface (P/N 1A4S), in (e, f) SAM surface (P/N 2A3C) and in (g, h) SP surface (P/N 3A5PS).

specimen 1B14S is a miniature specimen. The minimum in UTS and EAC initiation critical stress threshold was identified at the lowest nominal strain rate (1×10^{-7} s^{-1}).

3.5. Microstructural characterization of the near-surface region after CERT tests in the BWR environment

3.5.1. Microstructural characterization of the post-CERT-tested specimens at the widest cross-section

Figs. 15 and 16 show the representative microstructures of near surface region at the widest cross-section of the flat tapered specimens formed by oxide layer and deformation layer as function of the four machining surface treatments. This widest cross-section region had the lowest plastic deformation in the flat tapered specimen.

As shown in the Fig. 15(a, b), both discrete large crystallites and nano-flakes were detected at the outer oxide layer of the RS cross-section. A porous inner oxide layer with a thickness ranging from ~0.3 μm to ~1.0 μm was observed beneath the RS surface. The cross-sectional view associated with the STI surface showed a homogeneous inner oxide layer with a thickness of ~200 nm (Fig. 15(d)). The multiple deformation zones associated with machining were visible below the inner oxide layer of STI surface (SE image in Fig. 15(c) and BSE images in Fig. 16(c, d)). The thickness of the inner oxide layer associated with the SAM surface was ~400 nm and it appeared to be more uniform and homogeneous than that observed on the RS surface (Fig. 15(e, f)). The cross-sectional view associated with the SP surface is shown in the

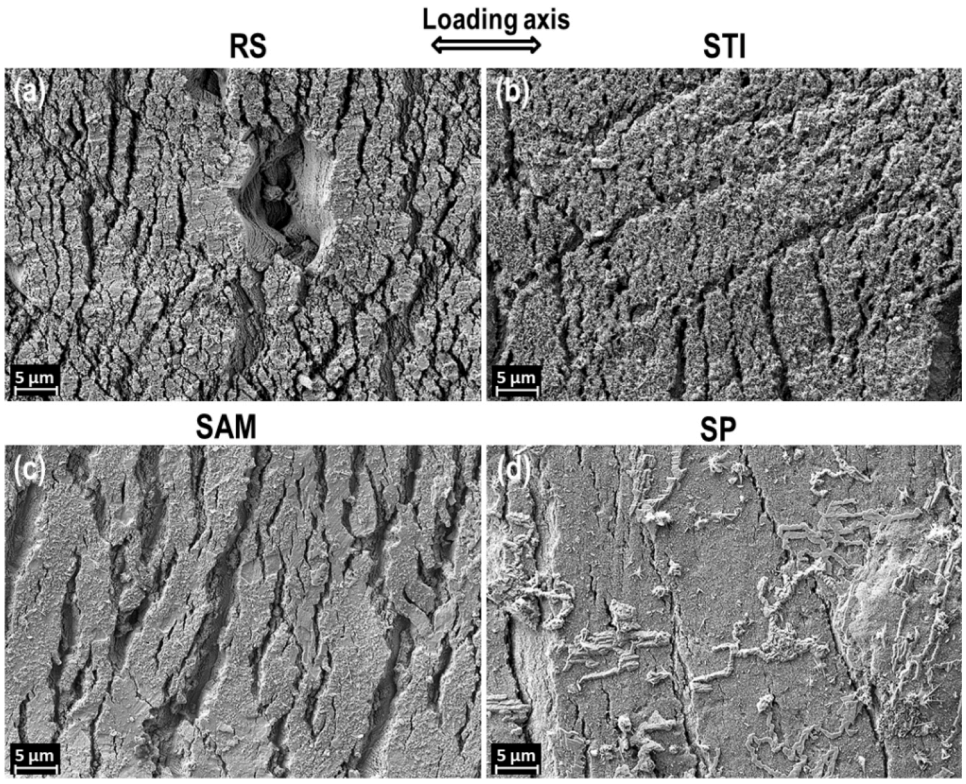

Fig. 11. SE images of surface oxide layer on the post-tested specimens from the narrowest cross-section (highest strain) for the four surface treatments. (a) RS surface (P/N 1B14S); (b) STI surface (P/N 1A4S); (c) SAM surface (P/N 2A3C); and (d) SP (P/N 3A5PS).

Fig. 15(g, h). An inner oxide layer ~500 nm containing numerous local fractures was observed. Cracks (marked with green arrows) that developed within the inner oxide layer, possibly related to severe plastic deformation of peening, are also shown in Fig. 11. Cracks generated by the peening process were also observed (Fig. 16(h)) in the near-surface region of the SP specimen at the widest cross-section.

Together with the BSE images in Fig. 16, EBSD analyses revealed the deformed structure beneath the surface at the widest cross-section (Fig. 17). The non-indexed area at the most upper part of the deformation area was due to the limited identification of the UFG layer by EBSD. These non-indexed areas were not due to large voids/cracks within the surface-deformed layers, as the large voids were not observed in Figs. 15 and 16. The RS surface treatment resulted in very limited deformation beneath the inner oxide, as shown in the corresponding IPF and KAM figures (Fig. 17(a, b)). The EBSD results associated with the near-surface region for the STI machined specimen is shown in Fig. 17(c, d). The images show a 3-layer structure deformation that extended ~4 μm in depth for the STI process. Specifically, the first layer adjacent to the machined surface was the UFG layer, which extended ~0.5 μm into the specimen; the second layer had a somewhat larger grain size (~0.5 μm) and was ~1.5 μm in thickness; and a third layer was ~2.5 μm thick with elongated deformed grains. A strong manufacturing deformation layer of ~6–7 μm with UFG was observed for the SAM surface (Fig. 17(e)). It was noted that the SAM specimen exhibited the highest average KAM values in the top 5 μm surface layer amongst all the surface treatments studied (Fig. 17(f)). The SP specimen exhibited a 2-layer manufacturing deformation structure (Fig. 17(d)), with a 2 μm thick UFG and a second deformed layer with a thickness of ~10 μm. The SP specimen exhibited a slightly coarser grain size in the near-surface deformed region compared to the STI surface. Some finely spaced shear bands were observed beneath the second machining deformation layer. These shear bands can be observed until ~120 μm from the surface.

For understanding the low apparent threshold stress of SP surface, BSE imaging was used for examination of the deformation structures at various locations from the surface at the widest cross-section of SP surface. Areas labelled b, c and d in the Fig. 18 were at a distance of 20 μm, 300 μm and 500 μm from the SP machined surface, respectively. The BSE image in Fig. 18(b) shows that the high density of dislocations changing into dislocation walls and forming dislocation cells by slip accumulation [25]. Fig. 18(c) exhibits planar slip characteristic with distance of 300 μm from the SP surface. The low-magnification cross-sectional EBSD of the tested specimen (P/N: 3A5PS) is shown in Fig. 19 (a), where the distribution of grain boundary (GB) misorientation is shown. The loading direction is horizontal, and the zone of maximum stress is on the right side of this image. The GBs with rotation angle between 5–15° and 15–65° have been marked with red and black colours, respectively. The GBs of through-the-specimen-thickness dendritic grains are characterized by a higher ratio of low-angle boundaries. A larger number of high-angle boundaries are observed in the area with smaller and uniform grains in the upper right area, which is associated with effect of multi-layer deposition process [20]. As revealed in Fig. 19 (b, c), peening-induced cracks were observed on the SP surface and the introduced machining deformation layer can be observed until ~120 μm from the surface.

3.5.2. *Microstructural characterization of the narrowest cross-section*

Characterization of cross-section metallographic samples also focused on the evaluation of the narrowest portion of the tapered tensile specimens in which the plastic deformation was highest, and the results for the various surface treatments are shown in Figs. 20–21. Several IG "cracks" (2 – 6 μm) were observed at the narrowest cross-section of RS surface, as shown in Fig. 20(a, b). Void formation was observed along a GB containing carbides (Fig. 20(b)). These IG carbides are preferential sites for void formation. In addition, fractured inclusions and coarse voids associated with inclusions were observed in Fig. 20(a). In Fig. 21 (b), strain localization at GBs and inclusions was most prominent in the KAM map at the RS surface.

Several shallow, blunt transgranular (TG) "cracks" (1 – 3 μm) were

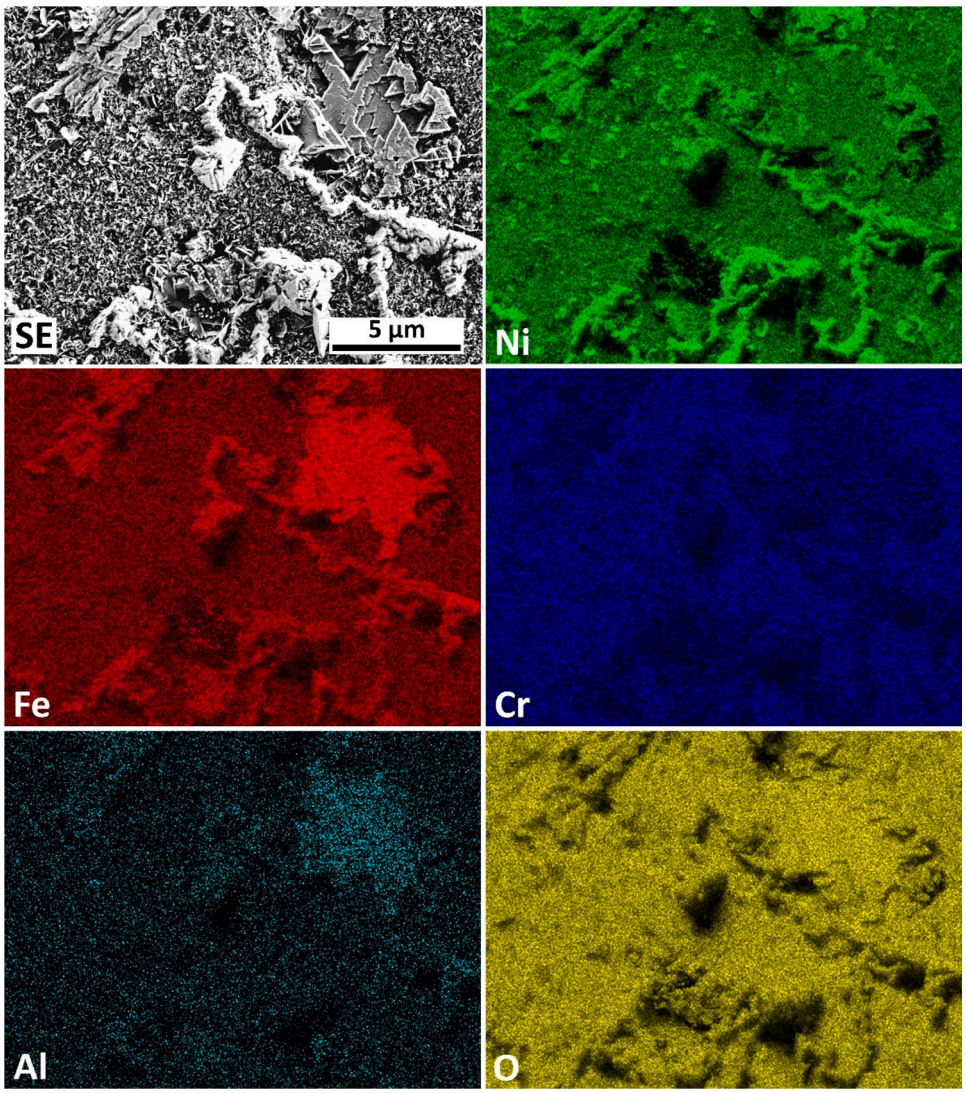

Fig. 12. SE image and corresponding low voltage (3.5 kV) SEM-EDX elemental maps for the Ni, Fe, Cr, Al and O from the surface oxide on the shot-peened Alloy 182 specimen (P/N 3A5PS) after the EAC test in simulated BWR environment.

observed at the STI surface in Fig. 20(c). Evidence of localized preferential TG oxidation was observed at the bottom of the blunt TG "crack" tip as shown in Fig. 20(d). Several deformation bands are shown (some with a width of 50 – 200 nm) in Fig. 21(c, d). In addition to the slip bands, low KAM was observed below the STI machined deformation layer.

Two sharp cracks (6 – 28 μm) and about 35 μm machined deformation layer beneath the surface were detected for the SAM surface treatment in Fig. 20(e, f) and Fig. 21(e, f). This crack propagated transgranularly through the machining-induced deformation zones (almost parallel to the loading axis) as shown in the IPF. Various TG cracks (>20 μm) with preferential oxidation were observed at the narrowest cross-section of SP surface (Fig. 20(g, h)). As seen in Fig. 21(g, h), the crack may propagate in linking up to void associated with hard and non-deformed inclusions. The summary of characteristic features of all surface treatments from the widest and narrowest cross-sections is present in Table 3.

4. Discussion

In this study, tests using the CERT technique were used to examine the EAC initiation susceptibility in flat tapered specimens of an Alloy 182 deposit as function of four surface preparations (RS, STI, SAM and SP). CERT tests involved dynamic plastic loading and so that these tests are more suitable for screening and comparison of large datasets [26], since they can provide a general trend of the EAC initiation susceptibility in a relatively short time. However, it is recognized that the limited duration of this accelerated test may not be suited to assess the precursor processes that can lead to EAC initiation in long-term component-relevant tests [19]. The results must be further verified, *e.g.* by constant load tests.

4.1. *Effect of the strain rate on the stress threshold*

In CERT tests, the severity of environmental degradation is mainly reflected by the duration of the test and by the strain magnitude. A lower calculated apparent EAC initiation stress threshold was determined for the lower nominal strain rate of 1×10^{-7} s^{-1} (Fig. 9), which was in good agreement with previous studies [27–29]. For a given strain, a lower strain rate results in a longer time for the environment to interact with the specimen surface; however, a higher strain rate produces greater dynamic strain with less time for environmental interaction and promotes mechanical failure. An enhancement of either factor may promote EAC initiation. In fact, for both RS and STI surface treatments, the increase in EAC initiation susceptibility at the lower strain rate (Fig. 9) was due to the prolonged exposure time that enables precursor reactions to

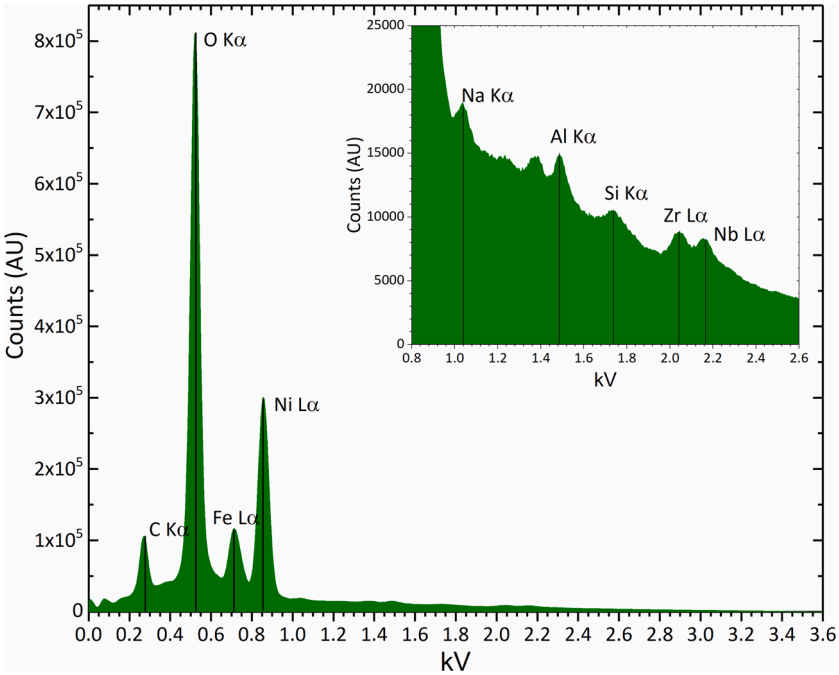

Fig. 13. Sum spectrum associated with Fig. 12 showing the main peaks associated with O (Kα), Fe (Lα) and Ni (Lα). The magnified inset from 0.8 kV to 2.6 kV shows the presence of small peaks associated with the presence of Al (Kα), Si (Kα), Nb (Lα).

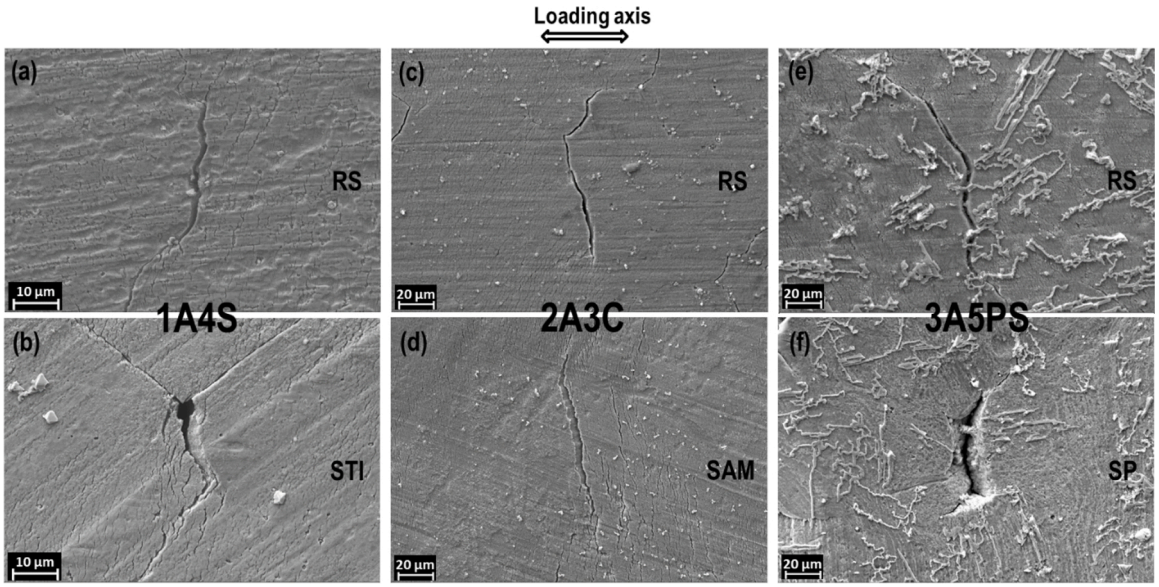

Fig. 14. (a – f) SE micrographs of the "last" identified cracks with a length of >20 μm for the Alloy 182 flat tapered samples exposed to simulated BWR environment; the loading direction is horizontal and the zone of maximum stress is on the left side of the images. (a, b) RS and STI surfaces of P/N 1A4S; (c, d) RS and SAM surfaces of P/N 2A3C; and in (e, f) the RS and SP surfaces of P/N 3A5PS.

occur as well as general oxidation. It is proposed that the EAC initiation for Alloy 182 under these environmental conditions is mainly controlled by the time-dependent oxidation process, whereas crack growth may be more dependent on the severity of mechanical loading. Boursier et al. [30] also reported that EAC initiation depends mainly on electrochemical processes, followed by a slow EAC propagation stage, influenced by stresses (residual and applied) on the surface.

4.2. Effect of the machining process on the EAC initiation and early crack growth

The surface machining processes on the Alloy 182 (from Figs. 3 to 7 and Fig. 21(e, f)) have generated different microstructures generally composed of an UFG layer and a subsurface deformed layer [11], as clearly observed from the ATEM analysis from Figs. 3 to 7 . The different machining processes have also generated different residual stresses states, thus affecting the EAC initiation susceptibility of the Alloy 182 [31]. Telang et al. [32] demonstrated that an increase in yield stress by peening induced deep compressive residual stresses and near-surface hardening from the increased dislocation density and refined sub-grains/grains, whose boundaries act as obstacles to dislocation glide. In addition, Bao et al. [16] concluded that the stronger EAC susceptibility could be related to the inhomogeneous distribution of defects such as high concentrations of dislocations near the surface layer and at

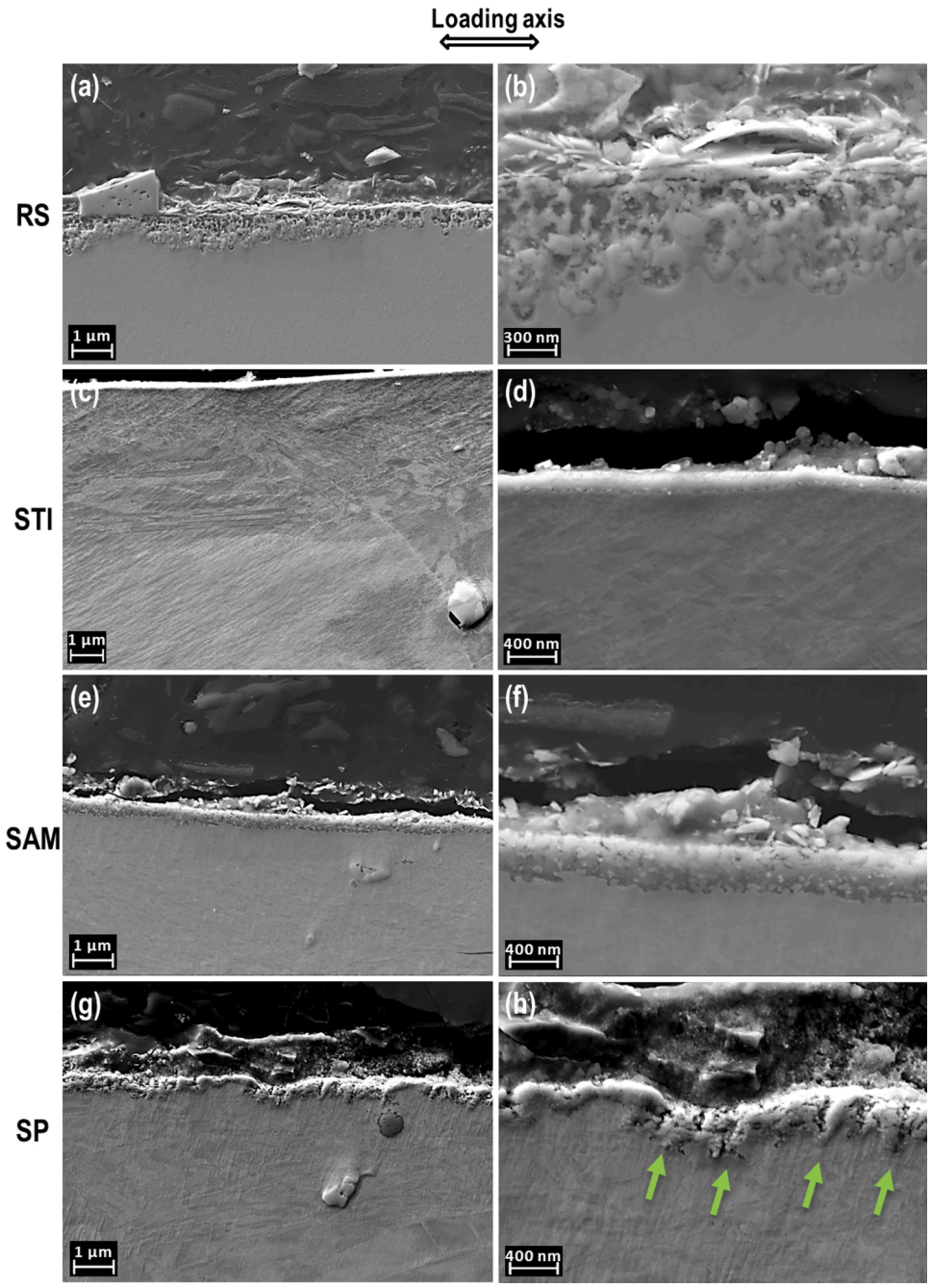

Fig. 15. SE images of the outer and inner oxide layer and the deformed layer from the widest cross-section of the oxidised flat tapered specimens as function of the different surfaces. (a, b) RS surface (P/N 3A5PS); (c, d) STI surface (P/N 1A4S); (e, f) SAM surface (P/N 2A3C) and (g, h) SP surface (P/N 3A5PS).

GBs.

During the machining process, dislocations are generated, resulting in the work hardening of surface layer. In the present work, the UFG layer, deformation bands (Fig. 17(h)) and accumulated dislocations in the hardened layer (Fig. 18(b)) can enhance the stress-induced diffusion and lead to further oxidation. The high GB area in the UFG layer and dislocations within the strain-localized sub-surface layer provide a quick path for oxygen diffusion [33]. Both the crack tip and the cold-worked surfaces are high stress regions with a high proportion of dislocations. Although the crack-tip stresses are the primary driving force for crack propagation, the residual stresses and defects in the machined surface layer can be the driving force for crack initiation by the formation of micro-cracks.

In addition, it has been reported that EAC susceptibility strongly depends on both GB chemistry [34] and misorientation [35–37]. An important factor that can affect EAC initiation is the difference in O and Cr diffusivities as a function of microstructure. It is well known that different microstructures can lead to different diffusion coefficients, thus influencing the oxidation and initiation of EAC cracks [38–40]. The RS surface exhibited a porous and slightly "wavy" inner oxide layer (Figs. 15 and 16). As shown by Zhai et al. [41], specimens with a 1200 grit finishes surface were less susceptible to EAC initiation than those polished to with a 1 μm finish. Another possible explanation of the thicker oxide layer in the machined prepared specimens (Fig. 15) can be associated with the different diffusion within the UFG layer. In fact, the diffusivity of the elements (*e.g.* O, Cr and Ni) in the UFG layer is significantly higher than that in a coarse-grained area due to the higher volume fraction of GBs and the decreased activation energy for diffusion

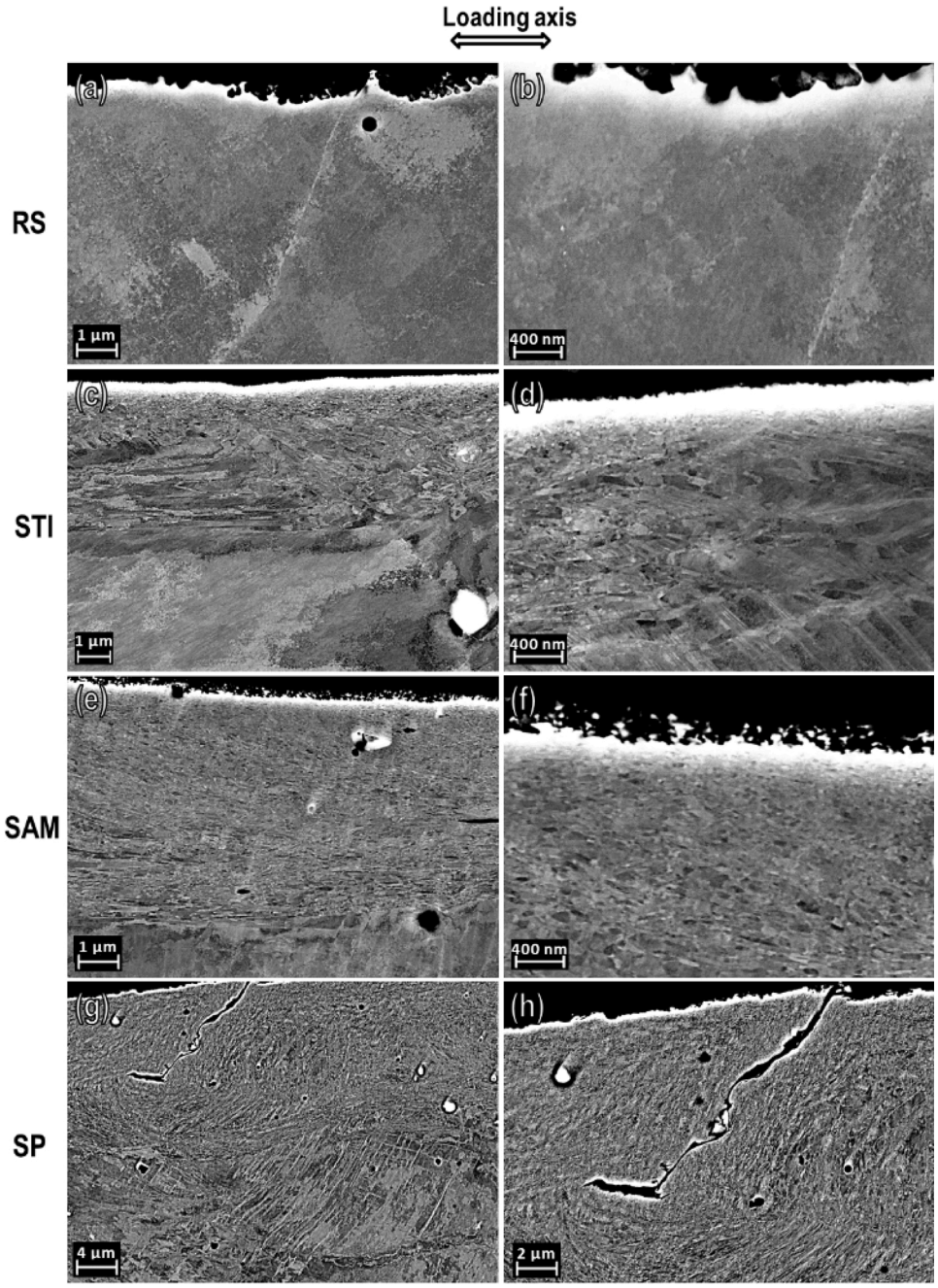

Fig. 16. BSE images of the deformed layer from the widest cross-section of the oxidised flat tapered specimens as function of the different surfaces. (a, b) RS surface (P/N 3A5PS); (c, d) STI surface (P/N 1A4S); (e, f) SAM surface (P/N 2A3C) and (g, h) SP surface (P/N 3A5PS).

in fine-grained or deformed materials [26]. In addition, the UFG layer can distribute deformation more uniformly, and thus reduce initiation susceptibility. It was also noted that the oxide layer was more compact and homogeneous on the SAM surface (Fig. 15) whereas a ruptured oxide film was observed on the SP specimen. The oxide layer on SAM surface present less preferential sites for crack nucleation compared to the SP surface. It is proposed that during CERT test, the micro-cracks associated with the very aggressive SP process led to a more pronounced oxidation and EAC crack initiation, when the compressive stress is relaxed due to straining.

It is also important to consider the CERT rate; at nominal strain rates of 1×10^{-6} or 5×10^{-6} s^{-1}, the RS surface has a stronger EAC initiation resistance than the STI surface. However, at a nominal strain rate of 1×10^{-7} s^{-1}, STI has a higher EAC threshold stress compared to RS surface. As discussed in chapter 4.1, EAC initiation is mainly controlled by the time-dependent electrochemical process. With the lower strain rate, the initiation of EAC was directly related to the preferential IG corrosion, which involves the penetration of oxidation through the surface oxide film to the GB. Therefore, the thick, porous RS surface oxide film will not inhibit the preferential oxidation of the GB whereas the UFG/deformed near-surface layers in the as-machined specimens will promote a more "uniform" oxidation of the surface and delay the IG oxidation of the A182. This may play a factor affecting the initiation of EAC, with the RS specimen exhibiting a lower EAC resistance than STI surface at 1×10^{-7} s^{-1}.

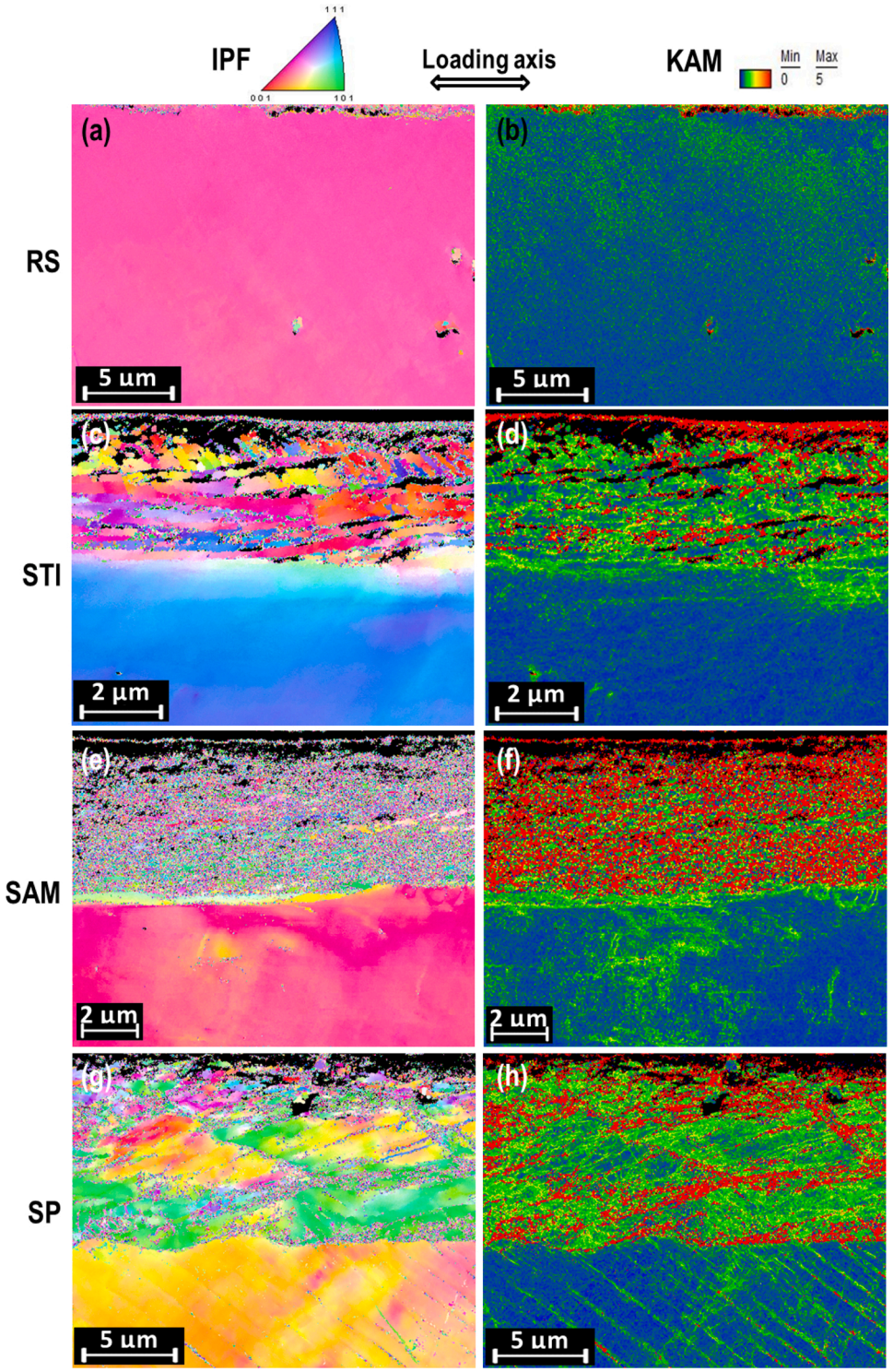

Fig. 17. EBSD maps obtained from the widest cross-section of metallographic cross-section samples of the post-CERT-tested surface-treated specimens: (a, b) RS surface (P/N 3A5PS); (c, d) STI surface (P/N 1A4S); (e, f) SAM surface (P/N 2A3C) and (g, h) SP surface (P/N 3A5PS). The IPF maps are shown in the top row and the corresponding KAM maps are shown in the bottom row; the intensity scale is in between 0° – 5°.

4.3. Effect of the oxides and inclusions on the EAC initiation and early crack growth rate in CERT tests

The general microstructural characterization of oxides formed on Ni-base alloys and their weld metals have already been reported in past studies [42,43]. Various oxides were detected in this investigation; the qualitative EDX results suggest that the flake-like oxides are most likely NiO whereas the coarser deposited particles may be $NiFe_2O_4$ [40]. Generally, a surface oxide has a lower ductility and a higher Young's modulus compared to the substrate [44] and therefore the oxide can fracture prior to the alloy matrix, thus promoting EAC initiation. The formation of a high number of inclusions and second phase precipitates (carbides) within this weld alloy (Fig. 20) is typical for Alloy 182 [45]. The inclusion in the Alloy 182 investigated were primarily Nb(C,N), Mg-Al spinel, SiO_2 and MnS. These inclusions may play a secondary role in the EAC initiation and propagation, as strain localization at the

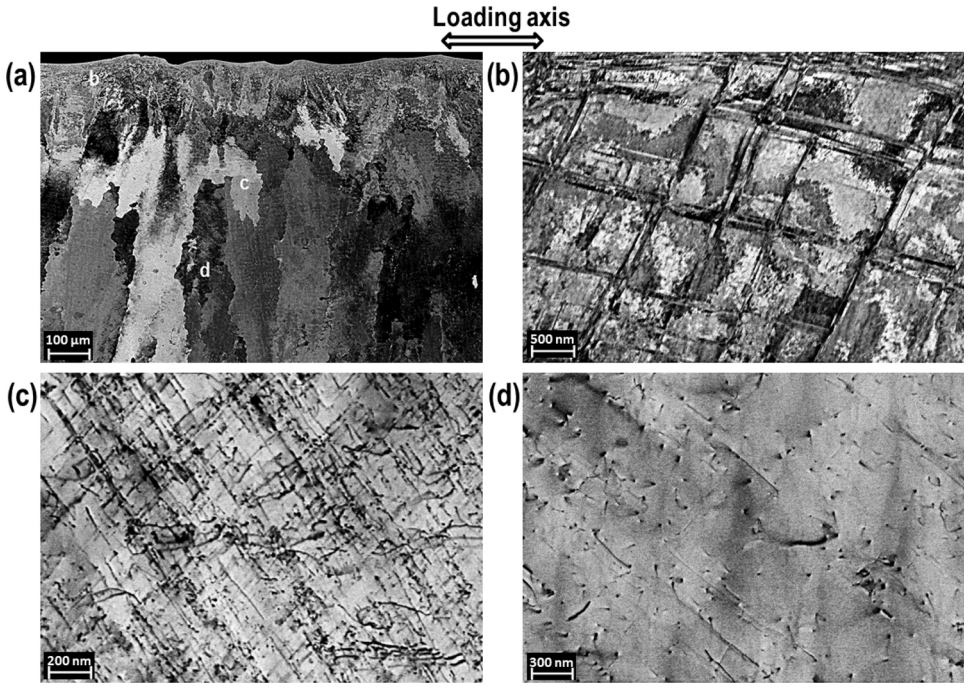

Fig. 18. BSE images of the deformed structure on the tested specimens with SP surface (P/N 3A5PS). (a) Low magnification image of the cross-section specimen showing the general microstructure; (b), (c) and (d) were with distance of 20 μm, 300 μm and 500 μm from the surface. Note the BSE images revealed dislocation structures due to channelling contrast.

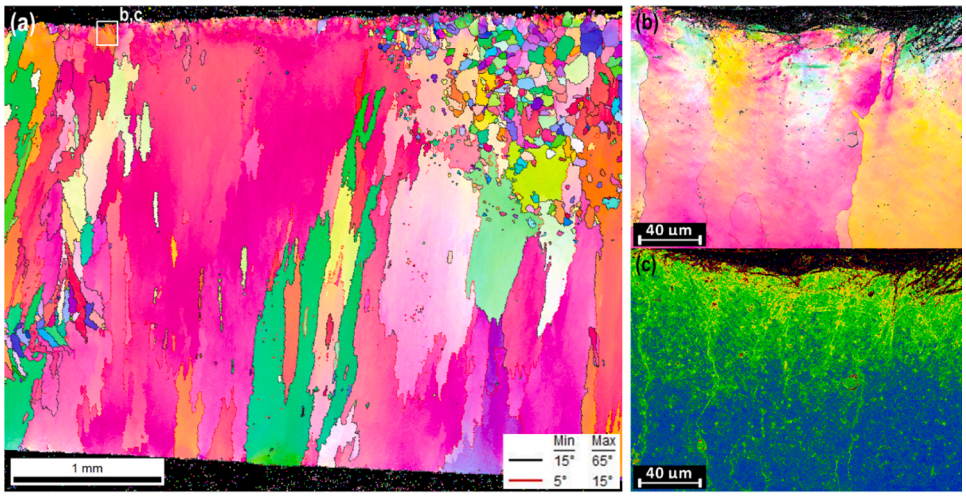

Fig. 19. (a) EBSD IPF and KAM maps of the specimen P/N 3A5PS cross-section after CERT test in simulated BWR environment. The loading direction is horizontal, and the zone of maximum stress is on the right side of the image. Upper surface was shot peened and the lower surface was polished. (b), (c) EBSD maps obtained from the SP surface as shown by insets in (a). The KAM intensity scale is in between 0° – 5°.

inclusion or at GBs may lead to fracture of the more brittle inclusions. It was also observed that the inclusions may be non-uniformly distributed/clustered so that EAC cracks might preferentially follow the ruptured inclusion clusters (Fig. 20(a, c, e, g)). Due to their higher ductility (compared to carbides/nitrides/oxides), MnS inclusions are normally not fractured, but they dissolve in elevated temperature water, thereby affecting the local environment. Very fine Mg-Al oxides have frequently been shown to nucleate TiN and Nb(C, N) inclusions in Ni-base welds. The fracture of the brittle Nb(C, N) inclusions under the tensile or shear strain produced by the dislocation slipping may contribute to local defect formation.

4.4. *Effect of SP on the EAC threshold stress*

Peening methods such as water jet/laser peening are recognized to be an effective method to mitigate EAC susceptibility [46–48]. The improvement of the SCC resistance by peening is attributed to the combined effects of both high-level compressive residual stress and grain refinement [47,48]. Kaneda et al. [49] compared surfaces treated with different types of surface treatment methods and concluded that shot peening resulted in the highest surface hardness and the strongest compressive stress of all methods included, which might lead to a high EAC resistance of SP surface. Sagawa et al. [17] reported for both Alloy 600 and weld Alloy 182 that the residual stresses prior to SP were 200–400 MPa due to grinding, but after the application of SP they became compressive and ranged from −200 to −1000 MPa at 20 μm

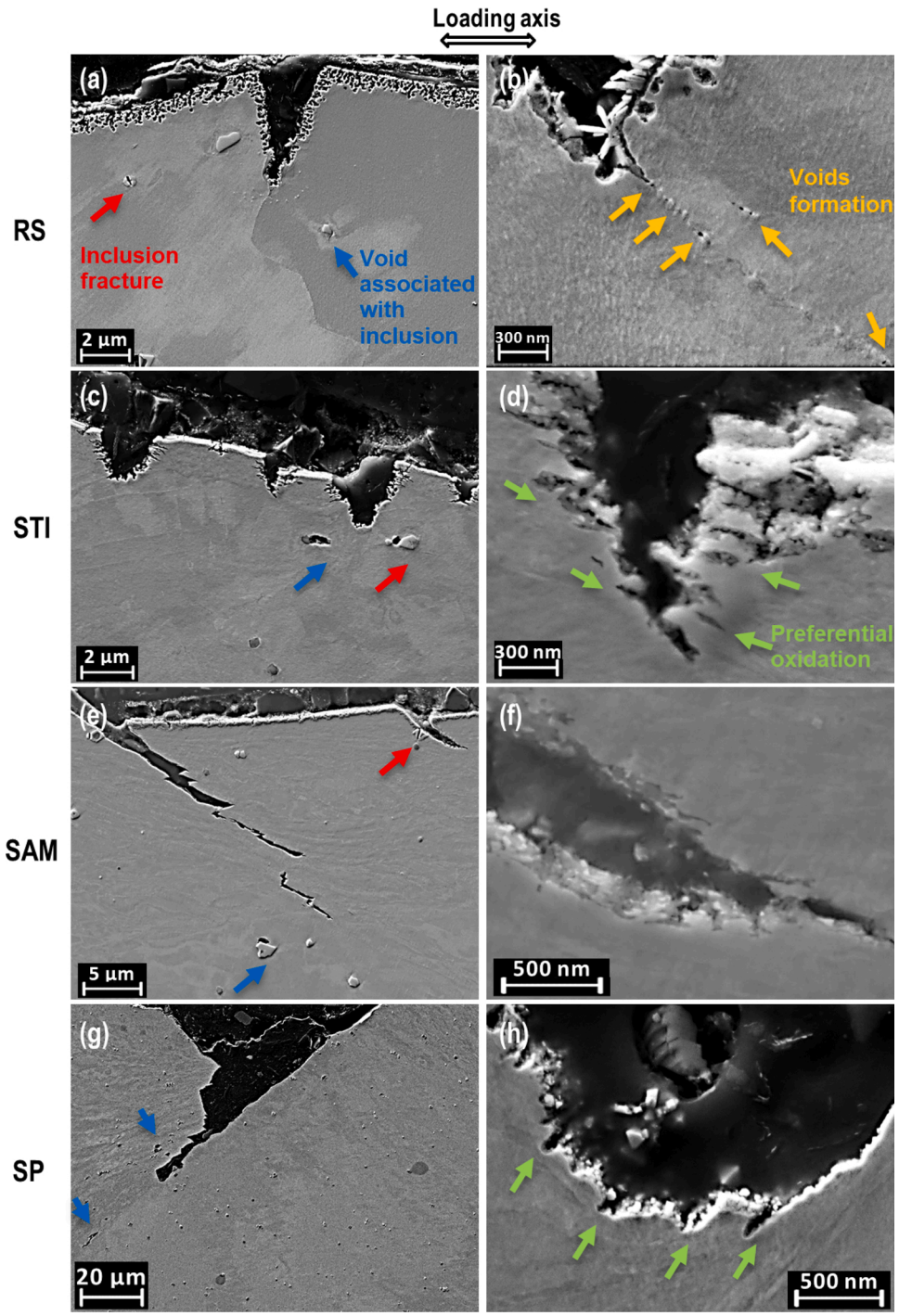

Fig. 20. SE images of cross-sectioned CERT-tested specimens for the various surface treatments. The imaged cracks were located in the narrowest portion of the tapered tensile specimens. (a, b) RS surface (P/N 3A5PS); (c, d) STI surface (P/N 1A4S); (e, f) SAM surface (P/N 2A3C) and (g, h) SP surface (P/N 3A5PS).

depth.

In this study, however, the tapered specimen with the SP surface exhibited the worst EAC resistance as assessed by the analysis of the tapered CERT specimens when compared with the other surface treatment (Fig. 9). The SP surface with its pre-existing cracks and intense local deformation as shown in Figs. 16(h) and 19 (b) and this kind of near-surface defects (pre-existing cracks) has already been observed in previous studies [50]. It must be noted that the CERT method can be considered as "aggressive" due to the active dynamic straining, which will relax the compressive residual stress induced by the shot peening process, thus not reflecting real component performance concerning the stress state, only the surface structure [51–53]. After the relaxation of the SP compressive residual stress, pre-existing flaws coupled with the plastically deformed near-surface layer and the hardened surface act as EAC initiation sites, thus explaining the lowest EAC resistance of the SP surface in this study. Deformation incompatibility also plays a role in crack initiation and propagation [35]. Strain localization at high-angle GBs on SP surface would also favour the EAC propagation. The EAC behavior of the SP specimen is consistent with previous studies that concluded that this process is not effective for mitigation in light water reactor environments, whereas other peening methods such as water jet and laser peening techniques are effective [50]. This present study has

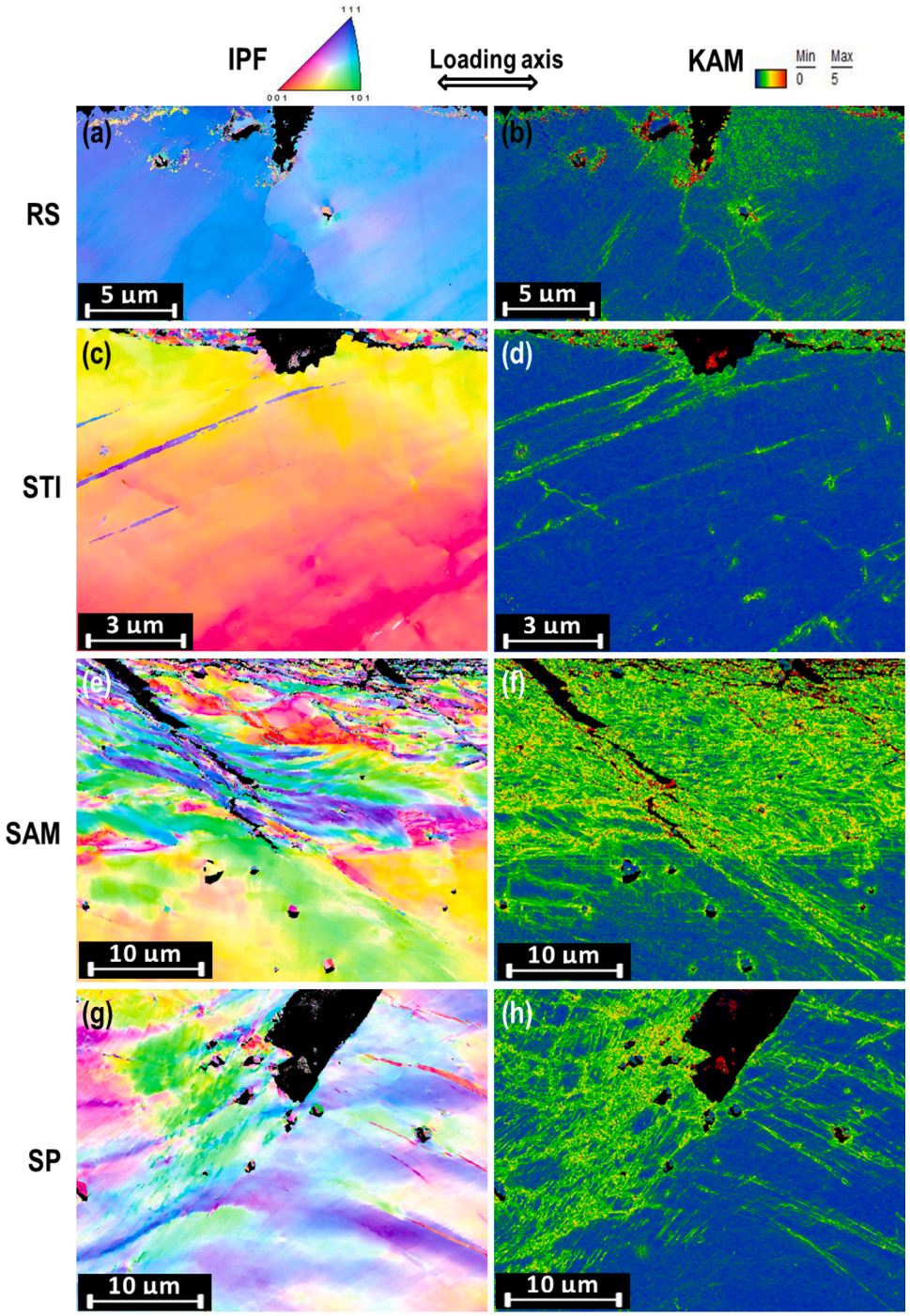

Fig. 21. EBSD IPF (top row) and KAM (lower row) maps obtained from metallographic cross-sections prepared from CERT-tested specimens the narrowest region of the tapered showing the localized deformation associated with the surface treatments and cracks. (a) RS surface (P/N 3A5PS); (b) STI surface (P/N 1A4S); (c) SAM surface (P/N 2A3C) and (d) SP surface (P/N 3A5PS. The KAM intensity scale is in between 0° – 5°.

provided the detailed microstructural evidence that demonstrates the severity of damage associated with the shot peening process.

5. Conclusions

The effect of surface condition (RS, STI, SAM, SP) on the EAC initiation and early crack growth in as-deposited Alloy 182 was evaluated after exposure to simulated BWR oxygenated high-purity water at 288 °C using the CERT method with flat tapered specimens at a nominal strain rate of 1×10^{-6} s^{-1}, 5×10^{-7} s^{-1} and 1×10^{-7} s^{-1}. The surface treatments, near-surface microstructure and oxidation on EAC crack initiation, growth and propagation were analysed from both the narrowest and widest cross-sections of tapered specimens tested at a nominal strain rate of 1×10^{-7} s^{-1} representing narrowest and largest strain, respectively. The main conclusions can be summarized as follows:

1 The apparent EAC initiation threshold stress increases with nominal strain rate, which indicates that higher EAC susceptibility can be found at lower strain rates. From these results, it is assumed that EAC initiation and early growth are mainly controlled by a time-dependent oxidation process.

Table 3
Summary of SEM observations from the post-CERT-tested tapered specimens as a function of surface treatment.

	Widest cross-section (lowest strain)		Narrowest cross-section (highest strain)	
Machined surface	Inner oxide layer	Manufacturing deformation layer	Deformation layer	EAC cracks
RS	Porous 300–1000 nm	Less than ~400 nm	Very limited and localized deformation	IG EAC
STI	Uniform ~200 nm	3 deformation layer (depth of ~4 μm)	Limited shear band formation	TG EAC
SAM	Uniform ~400 nm	Ultrafine-grained layer of ~6–7 μm depth	~35 μm thick deformation layer	TG EAC
SP	Cracked ~500 nm	2 deformation layer (depth of ~10 μm)	~50 μm thick deformation layer with strong shear band formation	TG EAC

2 The apparent EAC initiation susceptibility at a nominal strain rate of 1×10^{-7} s^{-1} for the different surface treatments rank as SP (most susceptible) > STI > RS > SAM (least susceptible), where the lowest threshold stress was found for the shot peened material. Shot peening-induced surface defects and the relaxation of residual stress are main reasons for the deteriorate EAC resistance of the SP surface. A compact, thick and homogeneous oxide layer was observed on the SAM surface. In contrast, RS surface was characterized by a non-compact, porous inner oxide of the main cause of lower EAC initiation resistance than the STI surface, which has the UFG layers and a layer of fine deformed grains.
3 Oxide formation affected by the surface microstructure and local fracture of inclusions may have played a secondary role in the initiation and crack growth of EAC cracks.
4 The CERT technique does not provide component-relevant quantitative data on EAC threshold values, but permits a ranking of the various surface treatments. The results must be further verified by, *e.g.,* constant load tests. The SP treatment is an extreme case in which the severe deformation/crack formation in the SP-surface layer has dominated the EAC results. It is further noted that the shot-peening process is not used in nuclear systems.

Author contributions

Study conception and design: Ehrnstén, Burke, Que and Volpe. Acquisition of data: Que, Volpe and Toivonen. Analysis and interpretation of data: Que, Volpe, Toivonen, Burke and Ehrnstén. Drafting of manuscript: Que, Volpe, Burke and Ehrnstén. Critical revision: Volpe, Burke, Ehrnstén and Que.

Data availability

The data that support the findings of this study are available from the corresponding author upon reasonable request.

Declaration of Competing Interest

The authors report no declarations of interest.

Acknowledgements

This project is funded by EU Horizon 2020 project MEACTOS from the EURATOM research and training programme 2014-2018 under grant agreement no. 755151. Support from the NUGENIA Mobility Programme under the grant number of 02/MG/2020 awarded to Z. Que is gratefully acknowledged. The authors would like to express their gratitude for the experimental contributions from T. Lehtikuusi and J. Lydman of VTT.

References

[1] S. Hwang, Review of PWSCC and mitigation management strategies of Alloy 600 materials of PWRs, J. Nucl. Mater. 443 (2013) 321–330.
[2] Y. Han, E. Han, Q. Peng, W. Ke, Effects of electropolishing on corrosion and stress corrosion cracking of Alloy 182 in high temperature water, Corros. Sci. 121 (2017) 1–10.
[3] Materials Reliability Program: GE Experience Report on Cracking in Alloy 182 (MRP-57): BWR Alloy 182 Stress Corrosion Cracking, EPRI Report, 2001.
[4] "IAEA TECDOC No.1471 "Assessment and Management of Ageing of Major Nuclear Power Plant Components Important to Safety: BWR Pressure Vessel Internals, International Atomic Energy Agency, Vienna, 2005.
[5] T. Shoji, Progress in the mechanistic understanding of BWR SCC and itsimplication to prediction of SCC growth behavior in plants, in: 11th International Symposium on Environmental Degradation of Materials inNuclear Power Systems-Water Reactors, Stevenson, Washington, USA, 2003.
[6] F. Ford, Quantitative prediction of environmentally assisted cracking, Corrosion 52 (1996) 375–395.
[7] Q. Peng, J. Hou, Y. Takeda, T. Shoji, Effect of chemical composition on grain boundary microchemistry and stress corrosion cracking in Alloy 182, Corros. Sci. 67 (2013) 91–99.
[8] R.W. Staehle, Clues and issues in the SCC of high nickel alloys associated with dissolved lead, in: 12th International Conference on Environmental Degradation of Materials in Nuclear Power Systems-Water Reactors, Salt Lake City, UT, United States, 2005.
[9] P. Andresen, P. Emigh, M. Morra, J. Hickling, Effects of PWR primary water chemistry and deaerated Water on SCC, in: 12th International Conference on Environmental Degradation of Materials in Nuclear Power Systems - Water Reactors, Snowbird, USA, 2005.
[10] R.W. Staehle, Quantitative Micro-Nano (QMN) approach to SCC mechanism and prediction-starting a third meeting, in: 15th International Conference on Environmental Degradation of Materials in Nuclear Power Systems — Water Reactors, Cheyenne Mountain Resort, Colorado Springs, CO (USA), 2011.
[11] L. Chang, L. Volpe, Y. Wang, M.G. Burke, A. Maurotto, D. Tice, S. Lozano-Perez, F. Scenini, Effect of machining on stress corrosion crack initiation inwarm-forged type 304L stainless steel in high temperature water, Acta Mater. 165 (2019) 203–214.
[12] L. Chang, M.G. Burke, F. Scenini, Understanding the effect of surface finish on stress corrosion crack initiation in warm-forged stainless steel 304L in high-temperature water, Scr. Mater. 164 (2019) 1–5.
[13] A. Turnbull, K. Mingard, J. Lord, B. Roebuck, D. Tice, K. Mottershead, N. Fairweather, A. Bradbury, Sensitivity of stress corrosion cracking of stainless steel to surface machining and grinding procedure, Corros. Sci. 53 (10) (2011) 3398–3415.
[14] N. Zhou, L. P, R. Pettersson, Surface characterization of austenitic stainless steel 304L after different grinding operations, Int. J. Mech. Mater. Eng. 12 (6) (2017).
[15] W. Zhang, K. Fang, Y. Hu, S. Wang, X. Wang, Effect of machining-inducedsurface residual stress on initiation of stress corrosion cracking in 316austenitic stainless steel, Corros. Sci. 108 (2016) 173–184.
[16] X. Zhong, S. Bali, T. Shoji, Effects of dissolved hydrogen and surface condition on theintergranular stress corrosion cracking initiation and short crackgrowth behavior of non-sensitized 316 stainless steel in simulated PWR primary water, Corros. Sci. 118 (2017) 143–157.
[17] W. Sagawa, T. Aoki, T. Itou, K. Enomoto, E. Hayashi, T. Ishikawa, Stress corrosion cracking countermeasure observed on Ni-based alloy welds of BWR core support structure, Nucl. Eng. Des. 239 (2009) 655–664.
[18] G. Bao, K. Shinozaki, S. Iguro, M. Inkyo, M. Yamamoto, Y. Mahara, H. Watanabe, Stress corrosion cracking sealing in overlaying of Inconel 182 by laser surface melting, J. Mater. Process. Technol. 173 (2006) 330–336.
[19] J. Bai, S. Ritter, H.-P. Seifert, S. Virtanen, Using tapered specimens to study the effect of hydrogen and surface finish on SCC initiation in Alloy 182 under boiling water reactor conditions, Corros. Eng. Sci. Technol. 52 (8) (2017) 558–566.
[20] R. Bosch, S. Ritter, M. Herbst, R. Kilian, M.G. Burke, Stress corrosion crack initiation testing with tapered specimens in high-temperature water – results of a collaborative research project, Corros. Eng. Sci. Technol. (2020).
[21] MEACTOS Project Website, 2021 [Online]. Available: https://meactos.eu/. [Accessed 2020].
[22] F. Scenini, J. Lindsay, L. Chang, Y. Wang, M. Burke, S. Lozano-Perez, G. Pimentel, D. Tice, K. Mottershead, V. Addepalli, Oxidation and SCC initiation studies of type 304L SS in PWR primary water, in: Proceedings of the 18th International Conference on Environmental Degradation of Materials in Nuclear Power Systems – Water Reactors, Portland, USA, 2017.
[23] J. Kenda, F. Pusavec, J. Kopac, Analysis of residual stresses in sustainable cryogenic machining of nickel based alloy—Inconel 718, J. Manuf. Sci. Eng. 133 (2011).
[24] A. Kanno, K. Hasegawa, F. Yoshikubo, R. Morinaka, H. Hatou, M. Tanaka, Development and field application experience of the reactor internal preventive maintenance technology, in: Third International Conference on Nuclear Power Plant Life Management, Salt Lake City, UT, USA, 2012.
[25] C. Yang, Z. Zhang, T. Cai, P. Zhang, Z. Zhang, Recovery of strain-hardening rate in Ni-Si alloys, Sci. Rep. 15532 (2015).

[26] L. Chang, M.G. Burke, F. Scenini, Stress corrosion crack initiation in machined type 316L austenitic stainless steel in simulated pressurized water reactor primary water, Corros. Sci. 138 (2018) 54–65.
[27] N. Totsuka, Z. Szklarska-Smialowska, Activation energy for IGSCC of alloy 600in an aqueous solution containing dissolved H2 at 300 to 350 °C, Scr. Metall. Mater. 45-47 (1987) 21.
[28] N. Totsuka, Y. Nishikawa, Y. Kaneshima, Effect of strain rate on primary waterstress corrosion cracking fracture mode and crack growth rate of nickel alloyand austenitic stainless steel, Corrosion 61 (2005) 219–229.
[29] W. Kuang, G. Was, The effects of grain boundary carbide density and strain rate on the stress corrosion cracking behavior of cold rolled Alloy 690, Corros. Sci. 97 (2015) 107–114.
[30] J. Boursier, D. Desjardins, F. Vaillant, The influence of the strain rate on the stress corrosion cracking of alloy 600 in high temperature primary water, Corros. Sci. 37 (3) (1995) 493–508.
[31] O. Chopra, W. Soppet, W. Shack, Effects of Alloy Chemistry, Cold Work, and Water Chemistry on Corrosion Fatigue and Stress Corrosion Cracking of Nickel Alloys and Welds, NUREG/CR-6721, ANL-01/07, Argonne National Laboratory, Argonne, IL, USA, 2001.
[32] A. Telang, A. Gill, S. Teysseyre, S. Mannava, D. Qian, V. Vasudevan, Effects of laser shock peening on SCC behavior of Alloy 600 in tetrathionate solution, Corros. Sci. 90 (2015) 434–444.
[33] S. Ghosh, M. Kumar, V. Kain, High temperature oxidation behavior of AISI 304L stainless steel - Effect of surface working operations, Appl. Surf. Sci. 264 (2013) 312–319.
[34] Q.J. Peng, H. Yamauchi, T. Shoji, Investigation of dendrite-boundary microchemistry in alloy 182 using auger Electron spectroscopy analysis, Metall. Mater. Trans. A 34A (2003) 1891–1899.
[35] J. Bai, S. Ritter, H. Seifert, S. Virtanen, Stress corrosion cracking initiation and short crack growth behaviour in Alloy 182 weld metal under simulated boiling water reactor hydrogen water chemistry conditions, Corros. Sci. 131 (2018) 208–222.
[36] P. Lin, G. Palumbo, U. Erb, Influence of grain-boundary-character-distribution on sensitization and intergranular corrosion of Alloy-600, Scripta Metall. Mater. 33 (9) (1995) 1387–1392.
[37] Q. Peng, T. Shoji, H. Yamauchi, Y. Takeda, Intergranular environmentally assisted cracking of Alloy 182 weld metal in simulated normal water chemistry of boiling water reactor, Corros. Sci. 49 (2007) 2767–2780.
[38] F. Scenini, R.C. Newman, R.A. Cottis, R. Jacko, Effect of surface preparation on intergranular stress corrosion cracking of alloy 600 in hydrogenated steam, Corrosion 64 (11) (2008) 824–835.
[39] L. O'Brien, R. Ballinger, D. Paraventi, L. Yu, Y. Maruno, P. Stahle, The effect of environment, chemistry, and microstructure on the corrosion fatigue behavior of austentitc stainless steels in High temperature Water, in: 17th International Conference on Environmental Degradation of Materials in Nuclear Power Systems – Water Reactors, Ottawa, Ontario, Canada, 2015.
[40] J. Panter, B. Viguier, J.-M. Cloue, M. Foucault, P. Combrade, E. Andrieu, Influence of oxide films on primary water stress corrosion cracking initiation of alloy 600, J. Nucl. Mater. 348 (2006) 213–221.
[41] Z. Zhai, M. Olszta, M. Toloczko, S. Bruemmer, Precursor corrosion damage and stress corrosion crack initiation in alloy 600 during exposure to PWR primary water, in: 17th International Conference on Environmental Degradation of Materials in Nuclear Power Systems - Water Reactors, Ottawa, Canada, 2015.
[42] C. Figueiredo, R.-W. Bosch, M. Vankeerberghen, Electrochemical investigation of oxide films formed on nickel alloys 182, 600 and 52 in high temperature water, Electrochim. Acta 56 (2011) 7871–7879.
[43] J. Bai, R. Bosch, S. Ritter, C. Schneider, H. Seifert, S. Virtanen, Electrochemical and spectroscopic characterization of oxide films formed on Alloy 182 in simulated boiling water reactor environment: effect of dissolved hydrogen, Corros. Sci. 133 (2018) 204–216.
[44] S. Ziemniak, M. Hanson, P. Sander, Electropolishing effects on corrosion behavior of 304 stainless steel in high temperature, hydrogenated water, Corros. Sci. 50 (2008) 2465–2477.
[45] Y. Lim, H. Kim, H. Cho, H. Lee, Microscopic examination of an Alloy 600/182 weld, Mater. Charact. 60 (2009) 1496–1506.
[46] S. Nishikawa, K. Ooi, M. Takahashi, T. Furukawa, Influence of shot peening and thermal ageing treatment on resistance to intergranular corrosion in shielded metal arc weld metal for type 600 nickel base alloy, Weld. Int. 31 (11) (2017) 837–845.
[47] J. Lu, K. Luo, D. Yang, C. Cheng, J. Hu, F. Dai, H. Qi, L. Zhang, J. Zhong, Q. Wang, Y. Zhang, Effects of laser peening on stress corrosion cracking (SCC) of ANSI 304 austenitic stainless steel, Corros. Sci. 60 (2012) 145–152.
[48] Y. Sano, K. Akita, K. Masaki, Y. Ochi, I. Altenberger, B. Scholtes, Laser peening without coating as a surface enhancement technology, J. Laser Micro/nanoeng. 1 (3) (2006) 161–166.
[49] J. Kaneda, H. Tamako, R. Ishibashi, H. Hato, M. Miyagawa, N. Yamashita, Effects of surface treatments on microstructure, hardness and resddual stress in type 316L stainless steel, in: 14th International Conference on Environmental Degradation of Materials in Nuclear Power Systems - Water Reactors, Virginia beach, USA, 2009.
[50] MRP-267, Revision 1: Materials Reliability Program: Technical Basis for Primary Water Stress Corrosion Cracking Mitigation by Surface Stress Improvement, EPRI Report, 2012.
[51] D. Buchanan, R. John, Residual stress redistribution in shot peened samples subject to mechanical loading, Mater. Sci. Eng. A 615 (2014) 70–78.
[52] R. Menig, L. Pintschovius, V. Schulze, O. Vöhringer, Depth profiles of macro residual stresses in thin shot peened steel plates determined by X-ray and neutron diffraction, Scr. Mater. 45 (2001) 977–983.
[53] A. DeWald, M. Hill, Eigenstrain-based model for prediction of laser peening residual stresses in arbitrary three-dimensional bodies part 2: model verification, J. Strain Anal. Eng. Des. 44 (2009) 13–27.